https://doi.org/10.5194/gmd-2022-88
Preprint. Discussion started: 22 April 2022

Geoscientific Model Development Discussions
Open Access

3D geological modelling of igneous intrusions in LoopStructural v1.4.4

Fernanda Alvarado-Neves[1], Laurent Ailleres[1], Lachlan Grose[1], Alexander Cruden[1], Robin Armit[1]

[1] School of Earth, Atmosphere and Environment, Monash University PO Box 28E, Victoria, Australia

Correspondence to: Fernanda Alvarado-Neves (Fernanda.alvaradoneves@monash.edu)

Abstract. Over the last two decades, there have been significant advances to improve the 3D modelling of geological structures by incorporating geological knowledge into the model algorithms. These methods take advantage of different structural data types and do not require manual processing, making them robust and objective. Igneous intrusions have received little attention in 3D modelling workflows, and there is no current method that ensures the reproduction of realistic intrusion shapes. Existing techniques are strongly dependent on the availability of data and manual processing to refine models. Intrusions are usually partly or totally covered, making the generation of realistic 3D models challenging without the modeller's intervention. In this contribution, we present a method to stochastically model intrusions based on the Object-Distance Simulation Method. We adapted this method considering typical datasets and rules of intrusion emplacement mechanisms. Using the geometric elements of intrusions (inflation direction, propagation direction) and stochastic simulations of intrusion thickness, we can generate realistic intrusions shapes while honouring observations and accounting for the spatial variability in thickness. The method is tested in synthetic and real-world case studies and the results indicate that the method can reproduce expected geometries without manual processing. A comparison with Radial Basis Function (RBF) interpolation shows that our method can better reproduce intrusion shapes, particularly when considering scenarios with sparse datasets.

1 Introduction

Significant advances in 3D geological modelling have shown how incorporating prior geological knowledge into interpolation algorithms can significantly improve the 3D representation of the geometry of structures (*e.g.*, Godefroy *et al*., 2017; Godefroy *et al*., 2018; Grose *et al*., 2018; Grose *et al*., 2019; Hillier *et al*., 2014; Laurent *et al*., 2013, 2016; Thibert *et al*., 2005). Geological knowledge of a geological feature can be incorporated to the 3D modelling workflow using different approaches. For instance, by parameterizing its 3D geometry, by defining its expected geometries, or by using complete structural datasets. Laurent *et al.* (2016) introduced a fold frame constrained by field observations that provides a parametric description of expected fold geometries within the entire model volume. The fold frame provides a spatial reference system for each deformation event, facilitating the construction of 3D models of poly-deformed terranes. Grose *et al.* (2017) used fold frame coordinates to characterize the geometry of folds with application to both synthetic and real case studies. A similar approach was proposed by Laurent *et al.* (2013), extended by Godefroy *et al.* (2018) and Grose *et al.* (2021b) to model faults, where a quantitative description of fault kinematics is incorporated into the modelling workflow. Godefroy *et al.* (2018) showed that

https://doi.org/10.5194/gmd-2022-88
Preprint. Discussion started: 22 April 2022

such an approach leads to significantly improved models compared to those based only on interpolation of data. The improvement was significant, especially in models built using few or poor-quality observations.

In the case of igneous intrusions, there are currently no methods that incorporate prior knowledge into the modelling algorithm. 3D models of intrusions are commonly characterized by a surface representing its contact boundary. This boundary is numerically described using the same frameworks as those used to build other geological interfaces such as stratigraphic contacts or faults. There are two main approaches to represent a surface within a geological 3D model (Wellmann and Caumon, 2018): (a) explicit methods, where geological surfaces are built by interpolating the points that lie on the surface, and these points and their arrangement directly define the surface, and (b) implicit methods, where a scalar field constrained by data points is interpolated, and geological interfaces are represented by equipotential surfaces of this scalar field. The best fit surface for observations of an intrusion relies on the data, interpolation approach and manual processing to refine the model. The quality and density of the input data vary depending on what data type is used to build the model. Typical datasets include surface observations, drilling data and modelling from geophysical surveys (*e.g.*, Braga *et al.*, 2019; Cervantes 2019; Eshaghi *et al.*, 2016; Rawling *et al.*, 2011). The estimated geometries are consistent with observations of the intrusions but do not include any geological rules and may not necessarily honour realistic intrusion geometries. Plutons, laccoliths, sills and layered intrusions develop tabular bodies, with their horizontal dimension greater than their vertical dimension (*e.g.*, Cruden *et al.*, 2017; Cruden *et al.*, 1999; McCaffrey and Petford 1997; Vigneresse *et al.*, 1999). The resulting 3D bodies built using data-driven methods might not honour these geometries without manual processing in sparse data environments. This is particularly important for 3D models of intrusions since they are usually only partly exposed if not totally covered and consequently inferred from geophysical interpretations or simulations, and intrusion observations (location and orientation of the contacts) are usually sparse. The estimation also does not assess the global uncertainty and spatial variability of the model (Haldorsen and Damsieth, 1990), which can be critical for models built with few or unevenly distributed data.

To address the problem of poor 3D representation of intrusions, we propose a general workflow based on the Object-Distance Simulation Method (ODSIM, Henrion *et al.*, 2008; 2010). Our method integrates conceptual knowledge of magma emplacement mechanisms into the ODSIM framework, enabling the reproduction of realistic intrusion geometries. As these concepts are integrated in the method, the results are objective and reproduceable. In practice, the method can use different types of datasets and build models of different types of intrusions, such as sills, plutons and laccoliths. The approach has two main steps. We initially build the intrusion network surface, an object representing the intrusion roof or floor contact. The network surface is constrained by host-rock mechanical anisotropies and incorporates knowledge of magma's mechanical behaviour into a purely geometric approach. The second step consists of modelling the extent of the intrusion body by utilizing the intrusion network object and a structural frame. This structural frame comprises a parameterization of the magma propagation and growth directions. We demonstrate the potential of this method with both synthetic and real-world case studies. We assess the value of this method by comparing the resulting 3D model of a sill intrusion with its 3D model built

https://doi.org/10.5194/gmd-2022-88
Preprint. Discussion started: 22 April 2022

Geoscientific Model Development Discussions
Open Access
EGU

using a classical interpolation framework. The results show that the method can reproduce expected intrusion geometries, even for sparse data scenarios.

2 Related work

2.1 Object-distance Simulation Method

The Object-distance simulation method (ODSIM) was developed to model geological bodies whose geometry is affected by pre-existing geological features (Henrion *et al., 2*008; 2010). It was initially tested on karsts and meandric channels, and used to model salt domes (Clausolles *et al., 2*019). The ODSIM simulates a stochastically perturbed 3D scalar field around a skeleton. The skeleton object can be constructed either in a deterministic fashion or by using object-based simulation when the target volume is poorly constrained. Examples of a deterministic approach would be using precise mapping of the karst cave to construct the skeleton representing the cave centre line. Object-based simulations are a good alternative when prior knowledge of the spatial distribution of the target body is available. When neither of these conditions is met, the skeleton can be built using stochastic simulations. Borghi *et al.* (2012) developed a method to simulate 3D karstic conduits as the minimum effort path between the inlets and outlets of a drainage system. The method considers the geological model of the study area, internal heterogeneities of the host rock and constraints from karsts genesis. The algorithm starts by parameterizing the geological model of pre-existing features. Then, a velocity field is computed within the volume of the model to represent mechanical anisotropies that may control the development of the karst. Different velocities are assigned to distinct geological features, generating a contrast between components that might be and might not be involved in the genesis of the karst system. A time map is computed with the velocity field, which is used to find the shortest path representing the most probable karst network.

A distance scalar field *D(p)* is computed around the skeleton, over the points of a previously defined grid *G*. The skeleton is defined implicitly as the isovalue 0 of the distance field *D(p)* on grid G, and the boundary of the geological body is defined by the isovalue λ of *D(p)*, where $\lambda \neq 0$. This scalar field could be any type of distance scalar field, including velocity fields, as proposed by Rongier *et al*. (2014). The scalar field *D(p)* is stochastically perturbed using a spatially correlated random field φ(p) that acts as a threshold for the target body's extent around the skeleton. The geological body is defined using an indicator function as follow:

$$I_B(p) = \begin{cases} 1 & if\ D(p) \leq \varphi(p) \\ 0 & otherwise \end{cases} \tag{1}$$

The data conditioning is obtained when φ(p) is higher than or equal to the distance between the data and the skeleton. It can be reached by transforming the data to threshold values after the simulation of φ(p), or using the data to condition φ(p) if using Sequential Gaussian Simulation (*e.g.*, Clausolles *et al., 2*019).

https://doi.org/10.5194/gmd-2022-88
Preprint. Discussion started: 22 April 2022

2.2 Structural frames in 3D implicit modelling

Following the conceptual ideas of Jessell *et al*. (2010), Laurent *et al.* (2016) introduced a structural frame for folds that provides a parameterization of the folded foliation at any point in the model. This parameterization enables the production of 3D models that honour both geological knowledge and structural data. In practice, this framework adds more constraints to a discrete implicit interpolation scheme, thus better reproducing folded geometries away from the data. The structural frame is constrained by field measurements, such as fold axis and fold axial foliation, allowing the model to use different structural data types.

The fold frame has three curvilinear axes, notated as $\tilde{X}$, $\tilde{Y}$, and $\tilde{Z}$ that correspond to the principal finite strain directions. Each axis is expressed as a 3D scalar field defined throughout the model, referred to as x, y, and z, respectively. Three local direction vectors e_x, e_y, and e_z are implicitly defined by the scalar fields, and describe the relative orientation of deformed foliations and structural elements. Two rotation angles plus these local direction vectors are used to define the local orientation of the folded foliation. Grose *et al.* (2017) developed a method to directly calculate these rotation angles from field observations of the folded foliation or lineation. A semi-variogram is used to test the periodicity of the folding within the structural frame coordinates. For distances smaller than the half-wavelength of the fold, the authors propose to use Radial Basis Functions to interpolate the angles between data points. For greater distances, the fold geometry can be fitted to periodic functions such as Fourier Series. The structural frame is critical in this workflow since the geostatistics are calculated in the fold frame coordinate system, allowing the assessment of the variability of the angles without the effects of younger deformation.

Laurent *et al.* (2013) presented a 3D curvilinear fault frame providing a parameterization of fault-related displacements that works as a basic fault operator. This method was tested in different geological settings with normal, reverse and strike-slip faults, obtaining kinematically consistent results. The fault frame has three coordinates described by three 3D scalar fields, representing a distance to the fault surface, the local normal to the fault and the slip direction, and a third coordinate orthogonal to the other two. Godefroy *et al.* (2018) developed a fault operator that extends this approach by adjusting it to stratigraphic data using numerical optimization.

Grose *et al*. (2021a) developed a generic structural frame that compiles both, the fold and fault frames frameworks described above. This generic structural frame is implemented in the open-source 3D modelling library LoopStructural (Grose *et al.*, 2021a, b). In LoopStructural, the generic structural frame has three coordinates that follow the major structural directions of the feature being modelled. The coordinates are interpolated sequentially, starting by the one which typically have more observations, *e.g.*, the first coordinate of the fault frame is the one that represents the fault surface. The second and third coordinates are interpolated using observations and orthogonality constraints. Structural frames are a key object in

https://doi.org/10.5194/gmd-2022-88
Preprint. Discussion started: 22 April 2022

LoopStructural that enables the modelling of complex geological features and differentiate the Loop platform from any other 3D modelling package.

3 Modelling igneous intrusions: general overview

This section describes the processes that control intrusion morphologies and how they are incorporated into the modelling approach. A detailed description of the algorithm and its implementation is presented in Section 5. Essentially, our method is based on the Object-Distance Simulation Method (ODSIM, Henrion *et al.*, 2008; 2010), adapted and modified to intrusions. An intrusion structural frame and conceptual models of the intrusion shapes are combined with the skeleton and spatially correlated random fields to constrain the geometry of intrusive bodies.

3.1 Arresting mechanisms of intrusions

Igneous intrusions comprise a significant volume of the Earth's crust and are found in all tectonic settings. They are part of Volcanic and Igneous Plumbing Systems, which involve magma production, transport and emplacement (Burchardt 2018). Magma production occurs due to partial melting of rocks in the upper mantle or crust (*e.g.*, Brown 2007; Petford *et al.*, 2000; van Wyk de Vries and van Wyk de Vries 2018). Magma can be vertically and laterally transported to its final emplacement location by the intrusion of dykes, sills and inclined sheets (*e.g.*, Brown 2007; Magee *et al.*, 2016). The emplacement of magma is controlled by mechanical interactions and the density contrast between the magma and its surroundings (*e.g.*, Brown 2007; Hutton 1988a; Petford *et al.*, 2000).

The emplacement of the magma is initiated when a vertically propagating magma conduit (*i.e.*, dyke) is arrested. Regardless of the magma composition and depth of emplacement, host rock heterogeneities and mechanical properties strongly control the intrusion location and final morphology. Examples of these heterogeneities are stiffness contrasts between adjacent layers (*e.g.*, Barnett and Gudmundsson 2014; Brun and Pons 1981), unconformities (*e.g.*, Hogan and Gilbert 1995), host rock discontinuities (*e.g.*, Clemens and Mawer 1992), stress barriers (*e.g.*, Barnett and Gudmundsson 2014), and shear zones (*e.g.*, Guineberteau *et al.*, 1987; Weinberg *et al.*, 2004).

For the purpose of 3D modelling, host rock heterogeneities such as geological contacts and faults can be described by surfaces. In the first step of our method, we define the intrusion network surface. This object is similar to the skeleton as per the ODSIM and represents the roof or floor contact of the intrusion. When the intrusion is poorly constrained by data, we adopt the method proposed by Borghi *et al.* (2012, see section 3.1) to build the intrusion network surface. The outcome is a simulated planar network of connected mechanical anisotropies that approximates the locations of the intrusion roof or floor contacts (Figure 1).

https://doi.org/10.5194/gmd-2022-88
Preprint. Discussion started: 22 April 2022

Geoscientific Model Development Discussions

In this step, it is important to understand the geometry of the pre-intrusion geology and its anisotropy as accurately as possible. Contacts, faults and foliations are fundamental because intrusions utilize these anisotropies to intrude the host rock and propagate (*e.g.*, Barnett and Gudmundsson 2014; Brun and Pons 1981; Clemens and Mawer 1992; Gudmundsson 2011; Morgan 2018; Souche *et al*., 2019). Observation points of the intrusion contacts are used to assess the anisotropies that were exploited during its emplacement. Where no observations are available, anisotropies can be simulated (using the user's geological knowledge of the area) and incorporated into the model. For example, if an intrusion has stepped up in the stratigraphy, but there are no observations of structures facilitating the step, a fault can be simulated and incorporated into the algorithm to build the intrusion network. A mechanical anisotropy can be simulated by sampling its orientation (*i.e.,* dip and strike) from a probability distribution and a range of values consistent with the local geology. Using these parameters, the anisotropy can be interpolated in a location provided by the modeller and incorporated into the algorithm when building the intrusion network. In this way, the intrusion geometry will be consistent with the surrounding host rock.

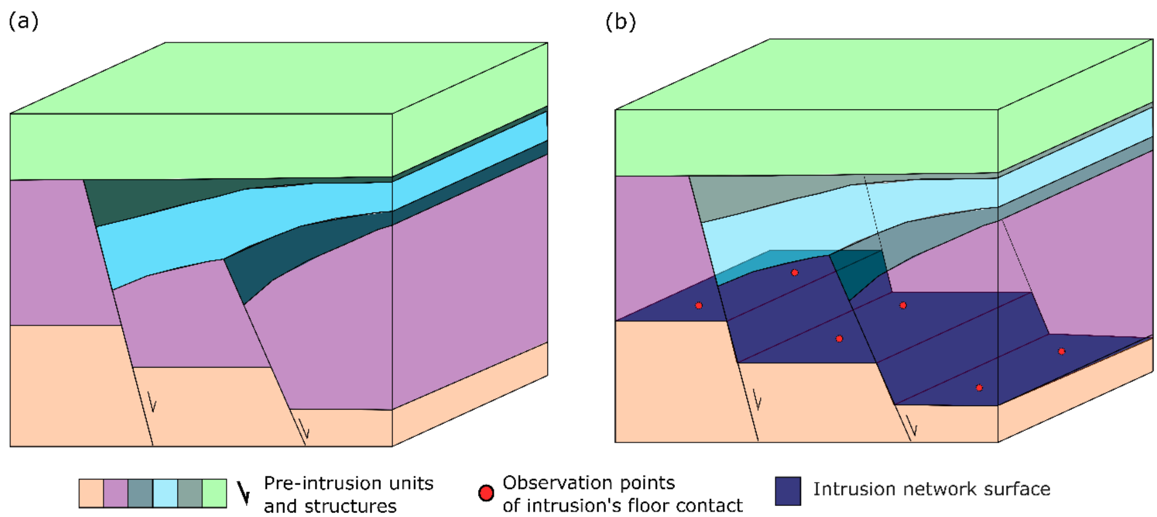

Figure 1. Schematic representation of the intrusion network surface. (a) Geological model of pre-intrusion units and structures. (b) Intrusion network of the model, constrained using intrusion's contact points (red dots).

3.2 Propagation of magma and intrusion growth

Once magma has been arrested, intrusion growth is controlled by host rock anisotropies until it reaches its maximum lateral and vertical extent. The growth of plutons depends on host rock mechanical properties (Cruden and Weinberg, 2018) and can occur by both vertical and/or lateral displacement of the host rock. (*e.g.*, Cruden 1998; Cruden *et al., 1*999; Grocott *et al., 1*999). Sills grow by horizontal propagation of their lateral tips and by vertical inflation (*e.g.*, Hutton 2009). If two or more sill segments propagate in the same direction but at different stratigraphic levels, they eventually coalesce, developing connectors such as steps or bridges (*e.g.*, Hutton 2009; Köpping *et al.*, 2021; Magee *et al.*, 2019; Schofield *et al.*, 2012). The sill inflation

https://doi.org/10.5194/gmd-2022-88
Preprint. Discussion started: 22 April 2022

Geoscientific Model Development Discussions
Open Access

direction is parallel to the intrusion opening vector, which may or may not be orthogonal to the intrusion plane (Magee *et al.*, 2019).

The concepts of propagation and intrusion growth are incorporated into the modelling method using a structural frame. The intrusion structural frame provides a curvilinear coordinate system for each intrusion sheet or pluton, similar to those used for the 3D modelling of faults and folds (Godefroy *et al.*, 2018; Grose *et al.*, 2021a, 2021b; Laurent *et al.*, 2013, Grose *et al.*, 2021a, Figure 2a), and it has three axes (Figure 2b). Axis $\tilde{G}$ is parallel to the inflation or growth direction of the intrusion, and is considered the major structural direction to interpolate the structural frame. Axis $\tilde{P}$, considered as the intermediate structural direction, is parallel to the propagation direction of the intrusion, and axis $\tilde{L}$ is orthogonal to the long axis of the intrusion or the propagation direction. The scalar fields relative to these axes, notated as g, p, and ℓ, respectively, are interpolated using an implicit discrete interpolation approach (*e.g.*, Caumon *et al.*, 2013; Frank *et al.*, 2007; Irakarama *et al.*, 2020), and are constrained using either field measurements or conceptual idea of their orientation.

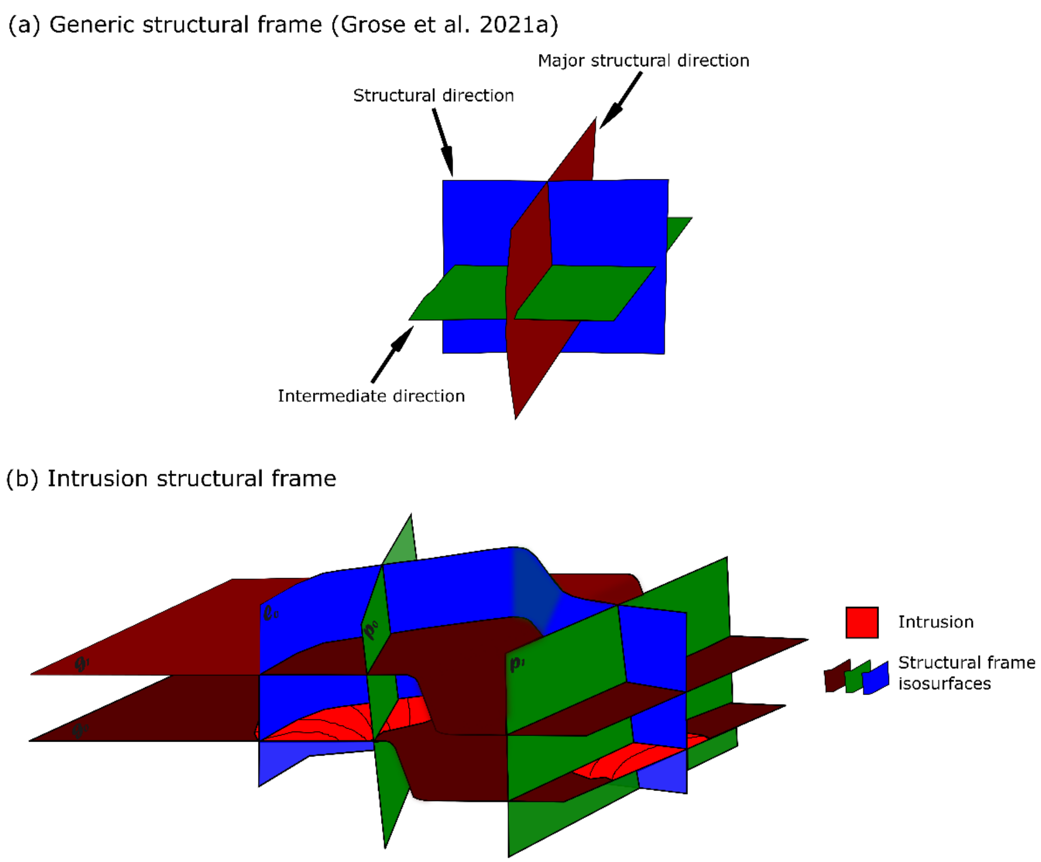

Figure 2. (a) Generic structural frame, figure from Grose *et al*. (2021a). (b) Schematic representation of the intrusion structural frame.

https://doi.org/10.5194/gmd-2022-88
Preprint. Discussion started: 22 April 2022

Geoscientific Model Development
Discussions

In general, intrusions develop specific shapes depending on their type. For example, most plutons, laccolith, sill and layered intrusions are described as having horizontal dimensions greater than their vertical dimension (*e.g.*, Cruden *et al.*, 2017; Cruden *et al.* .1999; McCaffrey and Petford 1997; Vigneresse *et al.* .1999). In cross-section, sills and dykes are planar sheet like intrusions (*e.g.*, Galland *et al.*, 2018; Jackson *et al.*, 2013; Kavanagh 2018), while plutons are frequently wedge or tablet-shaped (Cruden 2006; Cruden and McCaffrey 2001; Vigneresse 1995; Vigneresse *et al.*, 1999). Intrusions that are not tabular in shape are generally found in shear zones, which can facilitate the ascent and emplacement of the magma (*e.g.*, Hutton, 1988b; Guineberteau et al., 1987; Weinberg et al., 2004).

We identify specific geometrical figures to describe the broad scale shapes of different types of intrusions (Figure 3), namely a parallelepiped to describe a sill or an oblique cone to describe a wedge-shaped pluton. These geometrical shapes are parameterized using the structural frame coordinates and are used as conceptual models of the intrusion shape. To add variability to the intrusion boundary, we perturb these geometries using a spatially correlated random field conditioned to observation points of the intrusion contact. In this way, we reproduce realistic shapes of the intrusions accounting for field measurements and geological knowledge of magma systems.

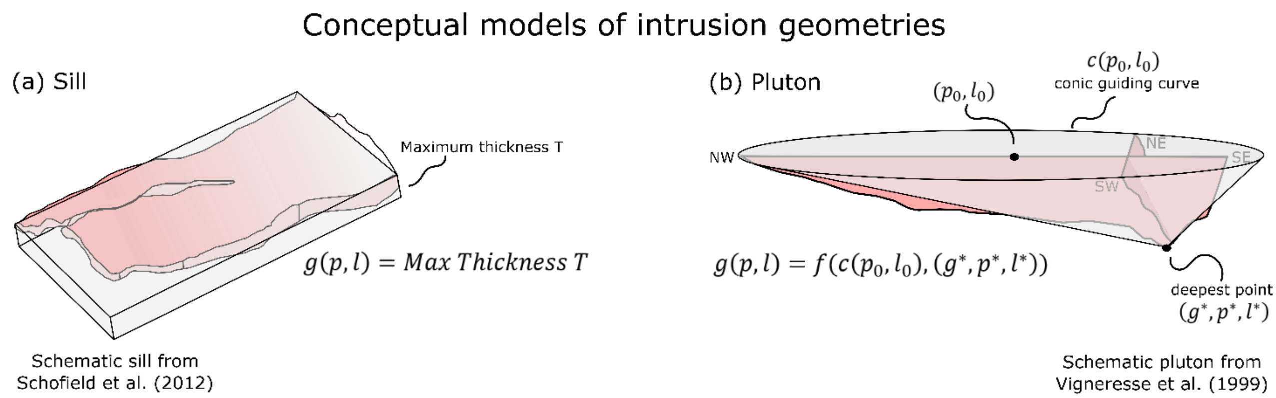

Figure 3. Examples of conceptual geometrical models of intrusions. (A) Schematic sill from Schofield *et al*. (2012). A parallelepiped is parameterized using the intrusion frame coordinates *(g,p,l)* and is used to represent the coarse scale geometry of the sill. (B) Schematic wedge-shaped pluton from Vigneresse *et al*. (1999). An oblique cone is parameterized using the intrusion frame coordinates *(g,p,l)* and is used to represent the coarse scale shape of the pluton. The pluton's deepest point corresponds to the vertex of the cone. These conceptual geometrical models are perturbed using a spatially correlated random field conditioned to the data, allowing to reproduce realistic intrusion shapes while honouring the spatial variability between the data points.

4 Algorithm and implementation

In this section, we describe the algorithm for the two steps of the method. In the first step, the modelling of the intrusion network is illustrated with a synthetic example of a sill complex (Case study 1, CS1), where a middle sill exploits a pre-existing structure and steps up in the horizontal stratigraphic sequence (Figure 4). The middle sill intrusion network is shown in Section

https://doi.org/10.5194/gmd-2022-88
Preprint. Discussion started: 22 April 2022

Geoscientific Model Development Discussions

4.1, and the final model, including the three sills, is shown in section 4.2. In this example, synthetic data of each sill roof and floor contact was used to build the model. Floor data points were used to stochastically simulate each intrusion network surface. The long axis of each sill was approximated using the spatial distribution of the data, and the growth direction was assumed to be perpendicular to the intrusion network.

For the second step, we demonstrate the workflow to model the Voisey's Bay intrusion, Labrador, Canada (Case study 2, CS2, Figure 5 and 6). For this example, we randomly sampled data from geological maps and cross-sections presented by Saumur and Cruden (2015) to reproduce a dataset composed of field measurements. The floor data points were picked from the drill holes in cross-sections. We assumed a horizontal stratigraphy and no post-intrusion deformation. Roof data points were used to simulate the intrusion network, and growth was assumed to be perpendicular to this surface. The intrusion long axis was approximated using the spatial distribution of the data.

At the end of Section 4 we present the 3D models of case studies 1 and 2 in Figures 7 and 8, respectively.

4.1 Intrusion network modelling: Case study 1 – Synthetic Sill Complex (CS1)

The first step of the method is to build the intrusion network surface. This object represents the approximate location of the intrusion roof or floor contact and can be obtained using a deterministic approach or stochastic simulations. Not using a skeleton per se is because intrusions are frequently not entirely exposed, and only roof or floor contact can be mapped, making it challenging to identify the centre line of a body.

A deterministic approach to obtain the intrusion network uses the top or base contact of a sill mapped on seismic images or the roof contour of a pluton mapped in the field. When the intrusion is poorly exposed, we suggest using the method developed by Borghi *et al.* (2012, Figure 4). The intrusion network is simulated as the shortest path connecting all the anisotropies that influenced the intrusion emplacement. To achieve this, we use a 3D implicit model of pre-intrusion units and structures, and observation points of the intrusion roof or floor contacts (Figure 4a). If the exact location of a fault is unknown, the fault can be simulated by sampling its orientation from a probability distribution defined by the modeller. The orientation parameters are then used to interpolate the fault surface, object that is added to the model and therefore considered when looking for the shortest path. The geology of the area is parameterized using a pre-defined grid G and indicator functions to differentiate between host rock and anisotropies that are significant for the intrusion emplacement (*e.g.*, geological contacts and structures, Figure 4b). The indicator functions are transformed into a velocity field using velocity parameters assigned to each type of anisotropy (Figure 4c). Borghi *et al.* (2012) highlighted that the velocity parameters should be interpreted only as model parameters. In the case of intrusions, the velocity parameters will generate contrast between geological anisotropies that are involved or not in the emplacement process. In other words, these values are determined arbitrarily by the user and do not represent the properties of the rock directly or any dynamic parameter of the emplacement but the relative ease of propagation

https://doi.org/10.5194/gmd-2022-88
Preprint. Discussion started: 22 April 2022

in a given direction. The model is divided into sections, and a time map is computed on each section using the velocity field and the Fast-Marching Method (Sethian 1999, Figure 4d). The Fast-Marching Method computes the time a front takes to arrive at any point of the section, starting from a boundary curve. The arrival time is obtained at each point of the grid G by solving the Eikonal equation:

$$\|\nabla T\| = \frac{1}{K} \tag{2}$$

where K is the speed of the front, and T is the arrival time of the front (Jones *et al.*, 2006). On each section, we define J_{in} and J_{out} as the points of intersection between an anisotropy of interest and each section's border. If more than one anisotropy intersects a section's border, then a temporal criterion of the emplacement can be used to define which of points in G will be J_{in} and J_{out}. J_{in} is defined using the anisotropy that was probably exploited first by the intrusion, and J_{out} using the anisotropy that was exploited last. The starting point to compute the time map is J_{out}.

Finally, the intrusion network is defined as the shortest path between J_{in} and J_{out}, starting from J_{in}. This path is computed on discrete sections and then joined to build the intrusion network surface (Figure 4e). The outcome of this step is a set of point within the intrusion network surface, and are stored in an indicator function $I_{NET}(x)$ as follow:

$$I_{NET}(\vec{x}) = \begin{cases} 1, if\ intrusion\ network\ is\ present\ at\ location\ \vec{x} \\ 0, otherwise \end{cases} \tag{3}$$

4.2 Intrusion body modelling: Case study 2 – Voisey's Bay intrusion (CS2)

As stated by the Object-distance Simulation Method (ODSIM, Henrion *et al.*, 2008; 2010), the representation of the geological body will be given by all the points found between the skeleton and a certain distance that varies along with the skeleton. For intrusions, the problem of identifying these distances can be translated into finding the intrusion thickness variation, *i.e.*, the distance between roof and floor contacts, and the intrusion width variation along its longitudinal axis.

To address this problem, we incorporate an intrusion structural frame into the ODSIM workflow. Threshold distances are stochastically simulated along the structural frame coordinates. These distances are used in the same sense as in the ODSIM, and the geological body is defined as the set of points that lie between these thresholds. Specifically, we define two sets of threshold distances. Thresholds distances to constraint the intrusion vertical extent related to its thickness variation, and threshold distances to constraint the intrusion lateral extent, related to the intrusion width variation.

https://doi.org/10.5194/gmd-2022-88
Preprint. Discussion started: 22 April 2022

Geoscientific Model Development
Discussions
Open Access
EGU

We use Sequential Gaussian Simulation to compute these threshold distances, so the spatial correlation between points is honoured. The examples presented in this contribution were carried out using the implementation of Sequential Gaussian Simulation available in the GeostatsPy python package (*https://pypi.org/project/geostatspy/*). The GeostatsPy library is a translation of the GSLIB: Geostatistical Library (Deutsch and Journel, 1998) functions to Python.

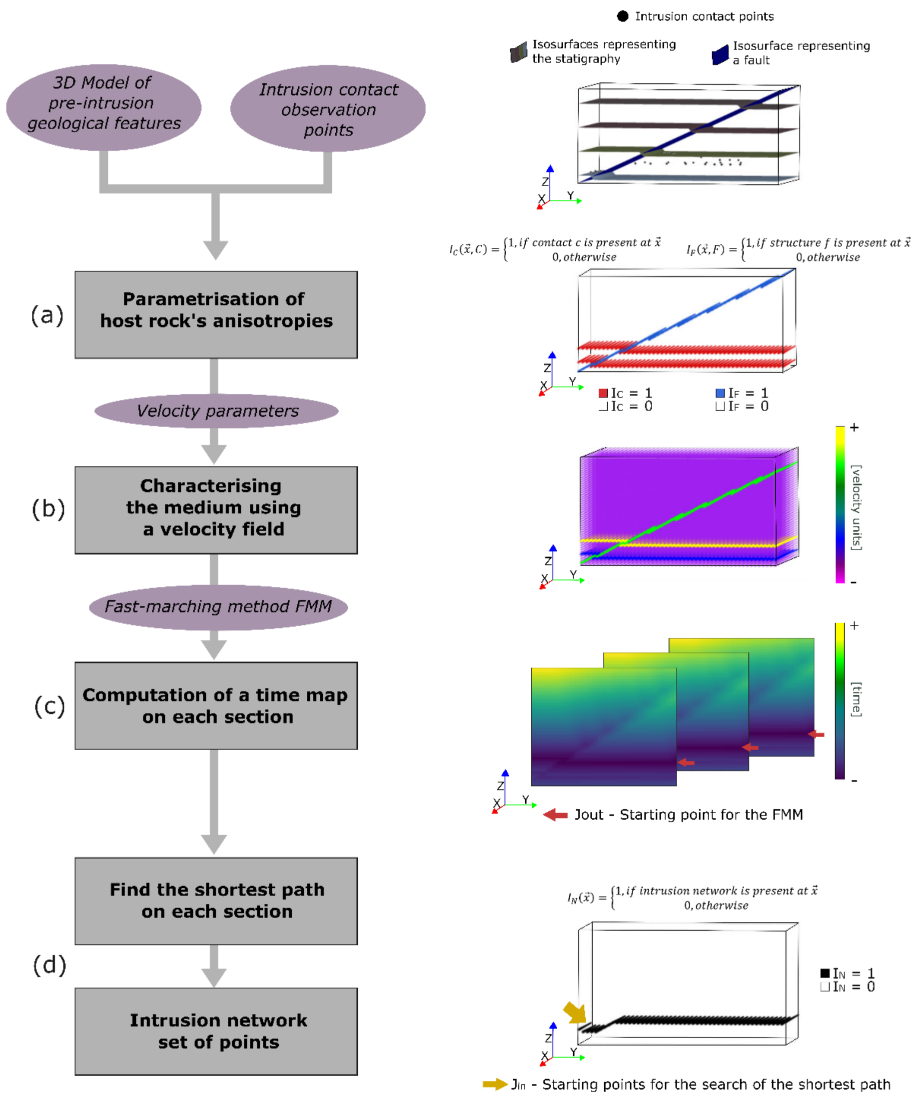

Figure 4. Workflow to build the intrusion network, modified from Borghi *et al*., 2012. The workflow is illustrated using CS1, a synthetic sill emplaced in a faulted sequence. (a) The geology of the area is parametrized using a pre-defined grid and indicator functions to differentiate between host rock and mechanical anisotropies significant for the intrusion emplacement. (b) The indicator functions are transformed into a velocity field using velocity parameters assigned to each type of anisotropy. (c) The model is divided into sections, and a time map is computed on each section using the velocity field and the Fast-Marching Method (Sethian, 1999). The starting point to compute the time map is J_{out} (red arrows). (d) Using the time map, the algorithm looks for the shortest path between the boundaries of the model, following the mechanical anisotropies. The stating points for the search is the shortest path is J_{in} (yellow arrow).

https://doi.org/10.5194/gmd-2022-88
Preprint. Discussion started: 22 April 2022

4.2.1 Interpolation of a structural frame for intrusions

As a reminder, the intrusion structural frame has three axes, denoted as $\tilde{G}$, $\tilde{P}$, $\tilde{L}$ that respectively correspond to the growth direction of the intrusion, propagation direction of the intrusion, and a direction orthogonal to the long axis of the intrusion. A distance scalar field represents each axis referred as $\boldsymbol{g}$, $\boldsymbol{p}$ and $\boldsymbol{\ell}$, respectively (Figure 5).

Coordinate $\boldsymbol{g}$ measures the distance to the intrusion network surface along $\tilde{G}$ and its gradient is parallel to the inflation or growth direction of the intrusion. If there are no inflation measurements, the gradient is assumed to be orthogonal to the intrusion network surface. Coordinate $\boldsymbol{p}$ represents a distance measured along $\tilde{P}$ from a reference point inside the intrusion. The gradient of this scalar field is a normalized vector parallel to the propagation direction of the intrusion. Coordinate $\boldsymbol{p}$ can be constrained using field measurements of the intrusion's propagation direction (*e.g.*, anisotropy of magnetic susceptibility measurements) or assumed parallel to the intrusion's long axis. Coordinate $\boldsymbol{\ell}$ measures a distance from the intrusion's long axis, and its gradient is orthogonal to coordinate $\boldsymbol{p}$ gradient.

The interpolation of the three intrusion frame coordinates is computed using a discrete interpolation technique (*e.g.*, Caumon *et al*., 2013; Frank *et al*., 2007). In this approach, the implicit function is calculated for each node of a pre-defined volumetric grid. The scalar field value at each node is obtained by solving a linear system constrained by data points where the scalar field value or its gradient is known. The structural frame is computed using LoopStructural (Grose *et al*., 2021a; 2021b), where the coordinates are interpolated using a discrete interpolator, *e.g.*, finite difference interpolator on a cartesian grid (Irakarama *et al*., 2020) or piecewise linear interpolation on a tetrahedral mesh (Frank *et al*., 2005, 2007). The coordinates are interpolated sequentially where $\boldsymbol{g}$ coordinate is interpolated first using the points of the intrusion network surface, which represent the isovalue 0 of this scalar field, and inflation measurements. The $\boldsymbol{p}$ coordinate is interpolated using observations of the propagation direction (or geological knowledge describing the propagation direction). Conceptually, the isovalue 0 of $\boldsymbol{p}$ coordinate should be related to the position of the intrusion feeder. However, for the purpose of the modelling, this isosurface can be anywhere in the model. The $\boldsymbol{\ell}$ coordinate can be interpolated using points along the intrusion long axis to represent its isovalue 0, and an additional constraint enforcing the orthogonality between $\boldsymbol{p}$ and $\boldsymbol{\ell}$. The scalar fields can be interrogated at any location of the model, so the ($\boldsymbol{g}$, $\boldsymbol{p}$, $\boldsymbol{\ell}$) coordinates are known for any point in the model.

https://doi.org/10.5194/gmd-2022-88
Preprint. Discussion started: 22 April 2022

Geoscientific Model Development
Discussions

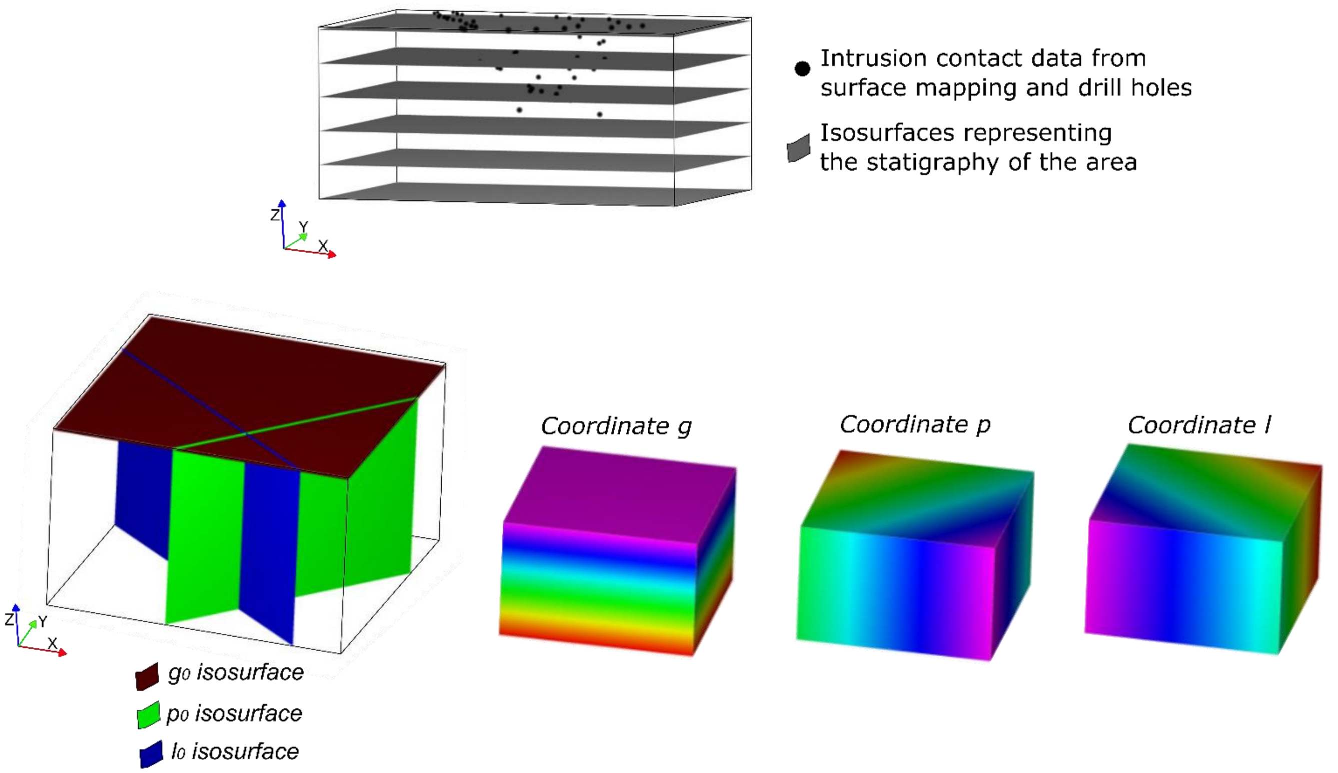

Figure 5. Structural frame of CS2, Voisey's Bay intrusion. Observation points were extracted from the geological maps and cross-sections presented by Saumur and Cruden (2015). The stratigraphy is assumed to be horizontal. Using the spatial distribution of the data, we approximate the intrusion long axis. Coordinate g is constrained using roof data points and an inflation direction perpendicular to the stratigraphy. Coordinate p is constrained assuming a gradient parallel to the long axis, and coordinate l is constrained using points along the long axis and a gradient perpendicular to the propagation direction.

4.2.2 Stochastic simulation of threshold distances

Once the structural frame is defined, we aim to find threshold distances that will approximate the boundary of the intrusion. Specifically, finding distances in $\tilde{L}$ along $\tilde{P}$ and distances in $\tilde{G}$ within $\widetilde{PL}$ will provide a comprehensive description of the intrusion boundary.

To find these threshold distances, we use Sequential Gaussian Simulations to compute three spatially correlated random field φ_{L1}, φ_{L2} and φ_G. These random fields represent the residual values given by the difference between a conceptual model of the expected intrusion shape and its actual shape. The spatially correlated random fields φ_{L1} and φ_{L2} are used to constraint the lateral extent to each side of the intrusion long axis, while φ_G is used to constraint the vertical extent. We identify two conceptual models for each intrusion: one to represent the intrusion geometry in $\widetilde{PL}$ (lateral extent) and one to represent its roof or floor geometry (vertical extent). The conceptual models are parameterized using the structural frame coordinates.

https://doi.org/10.5194/gmd-2022-88
Preprint. Discussion started: 22 April 2022

Geoscientific Model Development
Discussions
Open Access
EGU

Consider a set of observation points $i = \{1, \ldots, n\}$ and their respective (g_i, p_i, l_i) coordinates. The random fields are conditioned with the following residual values φi (Figure 6a):

$$\begin{array}{ll} \textit{Lateral extent} & \begin{aligned} \varphi_{L1}^{i}(p_i) &= \varsigma_{L1}(p_i) - l_i \\ \varphi_{L2}^{i}(p_i) &= \varsigma_{L2}(p_i) - l_i \end{aligned} \\ & \\ \textit{Vertical extent} & \varphi_{G}^{i}(p_i, l_i) = \varsigma_{G}(p_i, l_i) - g_i \end{array} \tag{4}$$

where φ_{L1} and φ_{L2} are the residual distances in $\tilde{L}$ along $\tilde{P}$ for each side of the intrusion, ς_L is the conceptual model of the intrusion geometry in $\widetilde{PL}$, φ_G are the residual distances in $\tilde{G}$ and ς_G is the conceptual model of the intrusion's floor/roof geometry. Examples of $\varsigma_s(p)$ are an ellipse for an elongated pluton or a rectangle for a sill. Examples of $\varsigma_g(p,l)$ are a cone for a wedge-shaped pluton or a parallelepiped for a sheet intrusion. The modeller must select the conceptual geometrical model according to prior knowledge of the intrusion type and local geology. A fourth random field g_{INet} is simulated to ensure the conditioning of the intrusion network contact to the input data used to build this object. The outcome of this simulation are distances to the intrusion network surface along the $\tilde{G}$ axis.

A probability distribution and a variogram control the simulation of each random fields. The distribution model is computed using the input data for each simulation, and is transformed to normal-score data for the simulation. The variogram can be customized by the modeller. However, we suggest using a variogram model that favours slight variability, so there are no sharp changes along the contact boundary. All our examples were built using isotropic variograms with infinite range and no nugget effect.

The simulations of the four spatially correlated random fields are performed in a pre-defined grid. The residual values are back-transformed into threshold distances (Figure 6b). For this, each point j of the grid is evaluated in the conceptual models ς_L and ς_G, and the threshold distances $l_{t1,t2}^{j}$ in $\tilde{L}$ and g_t^{j} in $\tilde{G}$ are given by:

https://doi.org/10.5194/gmd-2022-88
Preprint. Discussion started: 22 April 2022

Geoscientific Model Development
Discussions
Open Access

$$
\begin{aligned}
&\textit{Lateral extent} \quad && l_{t1}^{j}(p_j) = \varsigma_L(p_j) - \varphi_{L1}(p_j) \\
& && l_{t2}^{j}(p_j) = \varsigma_L(p_j) - \varphi_{L2}(p_j) \\
&\textit{Vertical extent} \quad && g_t^{j}(p_j, l_j) = \varsigma_G(p_j, l_j) - \varphi_G(p_j, l_j) \\
& && \forall\, (g_j, p_j, l_j) \in \mathit{Grid}
\end{aligned}
\tag{5}
$$

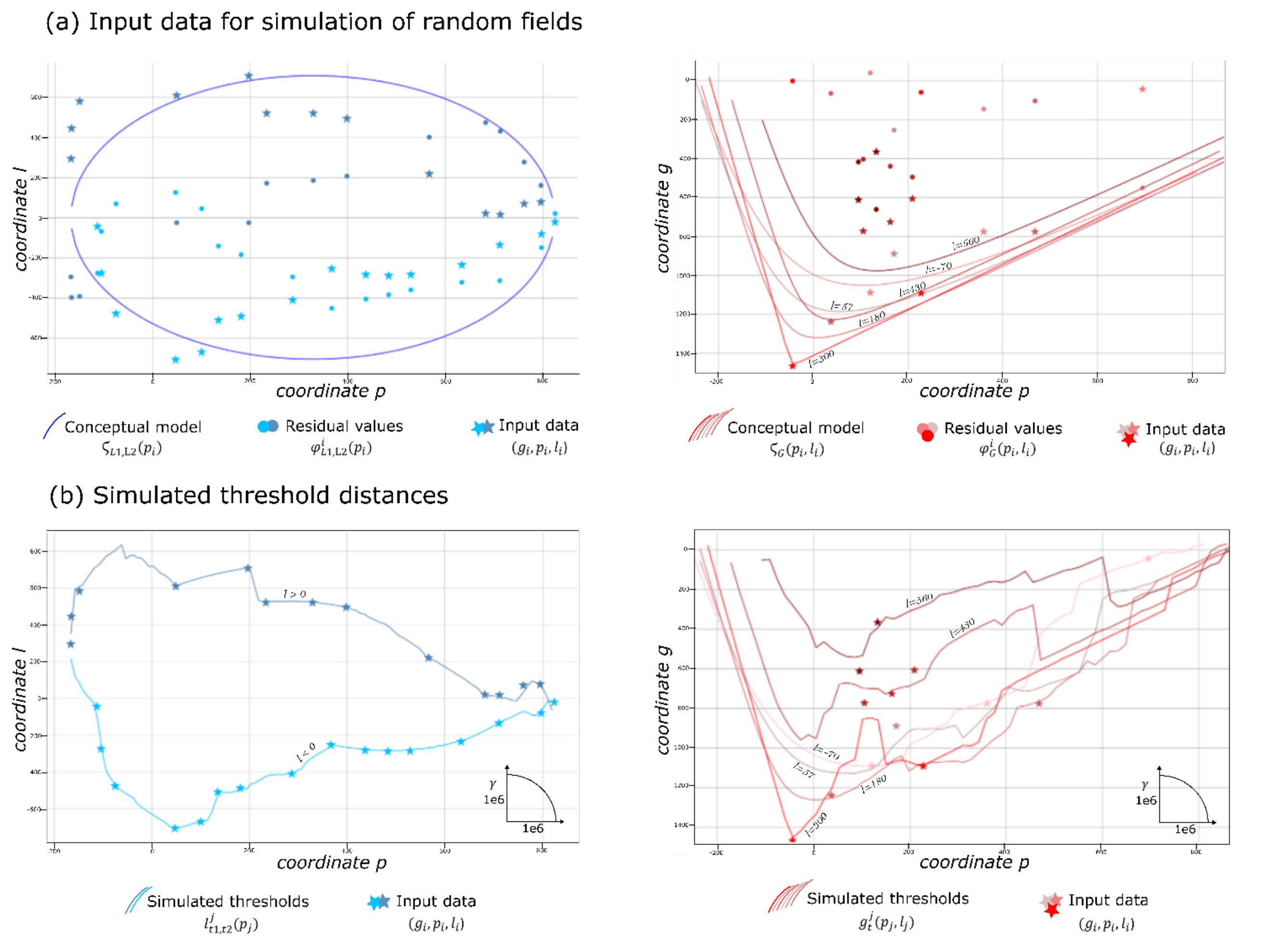

Figure 6. Example of spatially correlated random fields, Voisey's Bay intrusion. (A) Conceptual models and input data. In this example, the intrusion lateral extent (left plot) is constrained using an elliptical conceptual model (blue line) and residual values between the l_i coordinates of the observation points (g_i,p_i,l_i) and the conceptual model at p_i. The vertical extent (right plot) is constrained using an oblique cone conceptual model and residual values between the g_i coordinates of the observation points (g_i,p_i,l_i) and the conceptual model at (p_i,s_i). The red-tones lines represent the conceptual model and data along different l coordinates. (B) Resulting simulation after one realization. Both simulations were performed with an isotropic variogram model γ of infinite range and no nugget effect, which allow to obtain smoother surfaces.

https://doi.org/10.5194/gmd-2022-88
Preprint. Discussion started: 22 April 2022

Geoscientific Model Development Discussions
Open Access
EGU

The intrusion body is identified using an indicator function:

$$I_{Body}(g_j,p_j,l_j) = \begin{cases} 1 & if \;\; l_{t1}^j \leq l_j \leq l_{t2}^j \;\; and \;\; g_{INet} \leq \; g_j \; \leq g_t^j \\ 0 & otherwise \end{cases} \tag{6}$$

$$\forall \, (g_j,p_j,l_j) \; \in \; G$$

where 1 indicates the point (g_j,p_j,l_j) is inside the intrusion and 0 outside. The boundary of the intrusion is defined as:

$$I_{Boundary}\!: \{(g_j,p_j,l_j) \mid B(g_j,p_j,l_j) = 0\} \tag{7}$$

380

where B is a distance scalar field that combines the structural frame scalar fields minus the threshold distances, so the boundary of the intrusion is represented by the isosurface *B=0*, inside the intrusion B<0 and outside the intrusion B>0.

Figure 7 shows the resulting model of the CS1 (synthetic sill complex), and Figure 8 shows the 3D model of the CS2, Voisey's
385 Bay intrusion. This method is implemented in the *intrusion* module of *LoopStructural* (Grose *et al*., 2021a, b), and an intrusion can be built using the *create_and_add_intrusion* function from the GeologicalModel application programming interface.

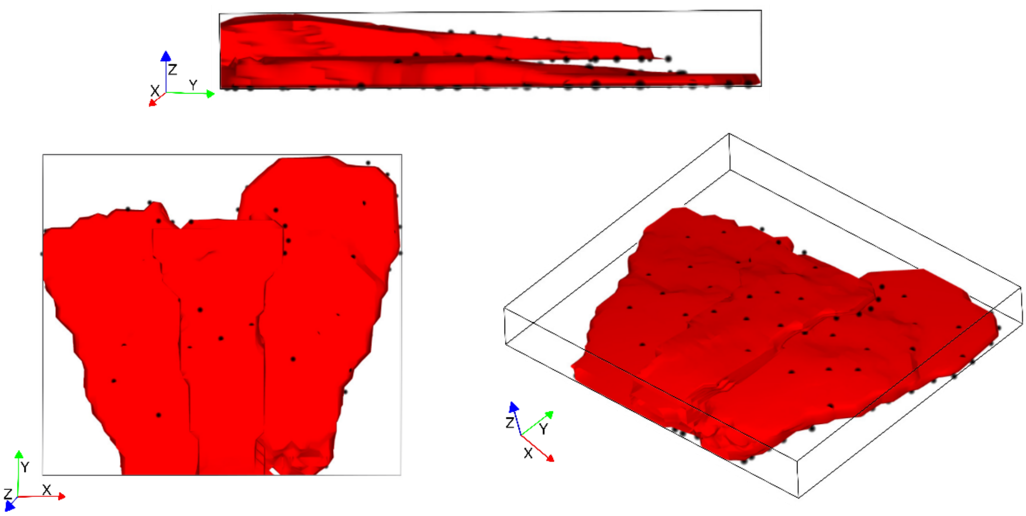

Figure 7. 3D model of CS1, synthetic sill complex. The red surface represents the sills boundary, and the black dots shows the location
390 **of the input contact points.**

https://doi.org/10.5194/gmd-2022-88
Preprint. Discussion started: 22 April 2022

Geoscientific Model Development Discussions

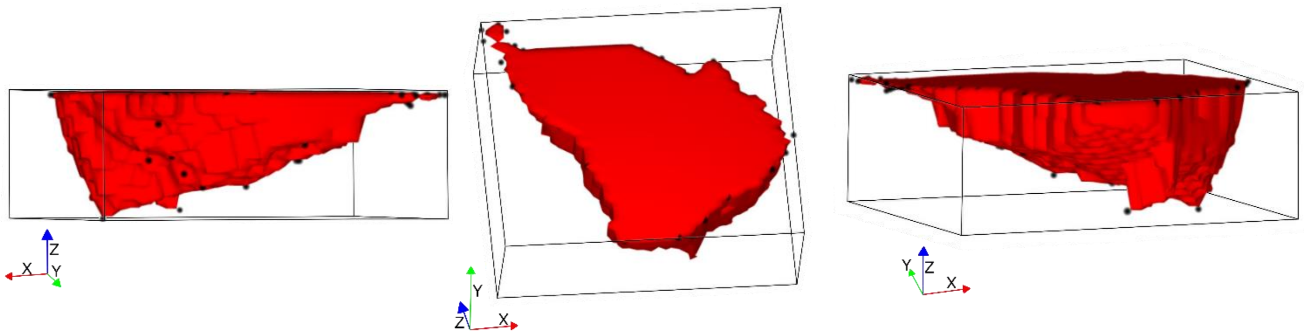

Figure 8. 3D model of CS2, Voisey's Bay intrusion, Labrador, Canada. The red surface represents the intrusion boundary, and the black dots shows the location of the observation contact points.

5 Case study 3 - Sill intrusion in NW Australia (CS3)

This last section assesses the value of modelling intrusions using structural frames and geometrical conceptual models by building four models (models A, B, C and D) of a sill intrusion in the offshore NW Australia shelf imaged in 3D seismic reflection data (Köpping *et al.*, 2021). The difference between the 3D models arises from the method used to build them and the amount and type of input data. Models A and B are built using an implicit surface interpolation approach, and they differ in the number of input constraints for each model. Models C and D are built using our proposed method, and the difference between them is that model D incorporates geometrical constraints from the emplacement history proposed by Köpping *et al.* (2021) for this sill.

The input data for the models is a sub-sample of the dataset presented by Köpping *et al.* (2021). The original dataset consists of the sill base and top contact points picked from seismic imagery and covers approximately 4042 km^2 with > 2.5 million data points (Figure 9a). According to Köpping *et al.* (2021, Figure 9), the intrusion is composed of a 13.4 km long, N-trending and strata concordant inner sill, which transitions into transgressive inward-dipping inclined sheets along its eastern margin and southwestern margin. Where inclined sheets are developed, the horizontal dimension of the inner sill is relatively narrow (~3.4 km). In the north section of the sill, where no inclined sheet is developed on the western margin, the inner sill widens up to 6.4 km, and has a convex-outwards and lobate western termination. The authors present a detailed characterization of the vertical thickness variation within the sill (Figure 9b). The eastern half of the inner sill is ~166 to ~249 m thick, rapidly decreasing westward to ~111 to ~166 m. The inclined sheets, the southern sill tip and the northwestern lobate termination are presented as tuned reflection packages, and their thickness can only be defined by the limits of separability and visibility of the data (~7 to ~56 m).

Köpping *et al.* (2021) propose an emplacement model for the sill, schematically represented in Figure 9c. The sill comprises one segment that propagated and inflated northward from a SW-NE trending fault, and another segment that propagated to the southwest of this fault. This SW-NE trending structure is located in the middle of the sill and likely also facilitate magma ascent. The transgressive inward-dipping inclined sheets formed along pre-existing faults in the east and south west. The straight geometry of the southwestern limb is interpreted to be controlled by pre-existing fractures and/or faults.

The pre-processing of the data, workflow and results of the four models are presented in the following subsections. The input data and resulting 3D models are presented in Figure 10.

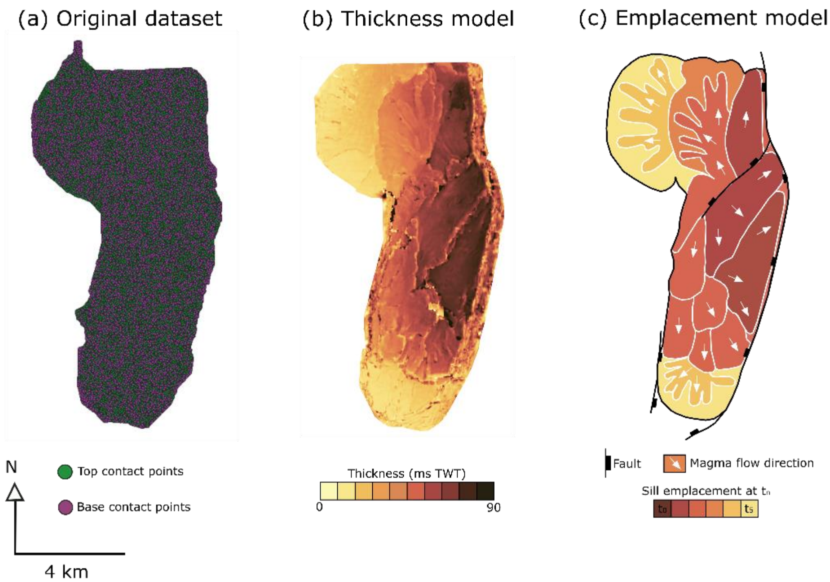

Figure 9. Data and models from Köpping *et al*. (2021): (a) Top and base contacts points picked on seismic images, (b) two-way time thickness model, and (c) schematic diagram of the emplacement history of the sill, in plan view.

Geoscientific Model Development Discussions

5.1 Model A and B - Radial Basis Function (RBF) implicit interpolation

Models A and B were built using *LoopStructural* (Grose et al., 2020, 2021a), specifically the *SurfE* interpolator. *SurfE* (*https://github.com/MichaelHillier/surfe*) implements a generalized radial basis function interpolator (Hillier *et al*., 2014). Radial basis function interpolation is a meshless interpolation and the scalar field can be constrained with different types of data, including value and gradient constraints. Models A and B are built using the signed distance interpolation of *SurfE* (single surface method).

The input data for these models consist of value and gradient constraints. In both models, the value constraints represent the intrusion contact location, and a value of 0 is assigned to each of these points. Gradient constraints correspond to vectors perpendicular to the stratigraphy with a direction towards the outside of the intrusion. For model A (Figure 10a), a sub-sample of approximately 0.1% of the original dataset is used as value constraints, and a selection of these points located in the strata concordant inner sill is used as gradient constraints. For model B (Figure 10b), we increase the amount of value and gradient constraints. In particular, the gradient constraints are distributed within the inner and outer sills.

5.2 Model C and D - Structural frame and conceptual models

Models C and D are built using our adaptation of the Object-Distance Simulation Method (ODSIM, Henrion et el. 2008, 2010) combined with structural frames and geometrical conceptual models. The main difference between these two models is that model D integrates geometrical constraints from the sill emplacement history proposed by Köpping *et al*. (2021). The resulting 3D models are shown in Figure 10.

The contact data for both models consist in a sample of approximately 0.1% of the original dataset, the same data points used for model A. These points are classified depending on their location as top, base and lateral contacts. The intrusion network of model C is interpolated using the sill's base contact points. To constraint the gradient of coordinate $\boldsymbol{g}$ of the structural frame, we use a selection of the input data points located in the strata concordant inner sill as inflation data, with a direction perpendicular to the stratigraphy towards the top contact. To constraint coordinates $\boldsymbol{p}$ and $\boldsymbol{\ell}$, we approximate the long axis of the intrusion considering the spatial distribution of the data. Points within the long axis represent the isosurface 0 of coordinate $\boldsymbol{\ell}$ and the propagation direction is assumed to be parallel to the long axis (Figure 10c).

For model D, we consider the sill as being composed of two segments emplaced at opposite sides of an NE-SW striking fault (Köpping *et al*., 2021, Figure 10c). The northern segment propagates into the fault's hanging wall towards the N-NW, while the southern segment propagates within the footwall towards the SE and then SSW. The two segments are modelled separately. For both segments, the intrusion network is built using a shortest path algorithm in order to include the effects of the marginal

https://doi.org/10.5194/gmd-2022-88
Preprint. Discussion started: 22 April 2022

Geoscientific Model Development
Discussions

faults on the sill geometry. To interpolate the structural frames coordinates, we used the same inflation data of model C, and propagation directions according to the emplacement history model (Figure 10d).

The simulations of both models are performed using isotropic variograms with infinite range and no nugget effect, and simple kriging. To simulate the lateral extents $l^{j}_{t1,t2}(p_j)$ we use an elliptical conceptual model $\varsigma_L(p_i)$ and lateral contact points. For the simulation of the top contact, we use a parallelepiped as the conceptual model $\varsigma_G(p_i)$ and the top contact points.

Geoscientific Model Development Discussions
Open Access
EGU

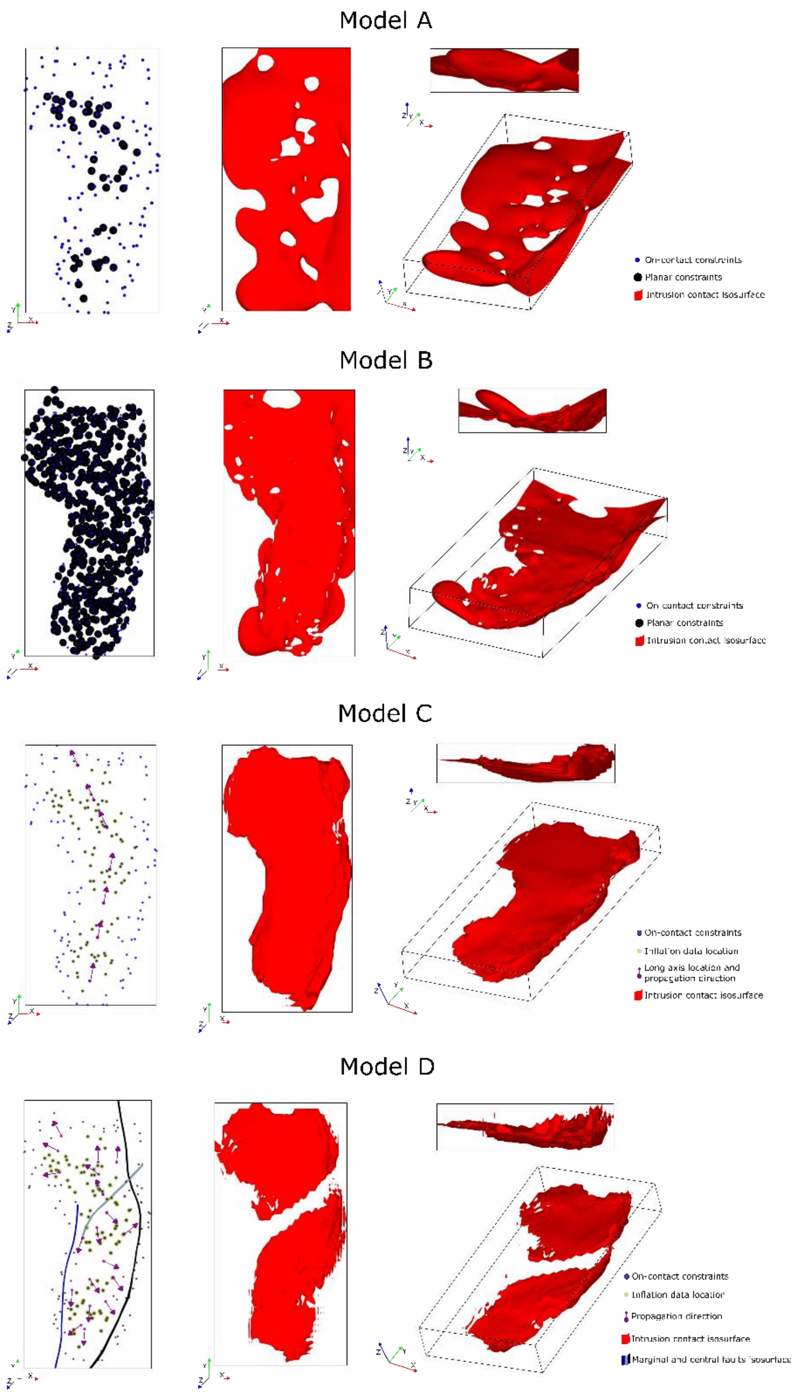

465 **Figure 10. 3D models of CS3, sill intrusion in the offshore Western Australia shelf. Models A and B were built using Radial Basis Function interpolation, and Model C and D were built using the method proposed in this work. To the left, plan view of the input data for each model. To the right, different views of the resulting 3D models.**

https://doi.org/10.5194/gmd-2022-88
Preprint. Discussion started: 22 April 2022

5.3 Comparison between the models

Visual inspection shows that, in general, RBF interpolation and our method can reproduce the coarse-scale geometry of the sill, with a N-trending inner sill transitioning to inward dipping outer sills. Considering the distribution of the data picked from seismic images (Figure 9a, Köpping *et al.*, 2021), our method is more accurate at constraining the shape of the terminations of the sill, while the RBF interpolation extrapolates the isosurface that represents the intrusion contact away from the data. This is exacerbated in model A due to the reduced input data compared to model B. In RBF interpolation, the value of the basis function depends on the distance $\|x - x_i\|$ where x is the position to evaluate the function and x_i the location of the data point, which may generate blobby geometries away from the data (Wellmann and Caumon, 2018). Models A and B present holes within the intrusion related to the absence of on-contact or planar constraints. Models C and D do not capture some of the sill thinnest parts, such as the southern tip, the northwestern lobate termination and the eastern inclined sheet of the northern segment of model D. In these areas, the grid elements have larger dimensions than the width or length of the sill, and therefore the isosurface represented by B=0 (see section 4.2.2) is not captured in the scalar field values assigned to each grid nodes. This occurs in more extensive areas in Model D, specifically the northern segment's eastern and western margins. As the simulations were performed using variograms with infinite range and search radius covering the entire intrusion body, the threshold values depend on the whole input dataset of each model. While model C thresholds reflect the effects of both the southern and northern segments data, model D thresholds are restricted to the data of each segment.

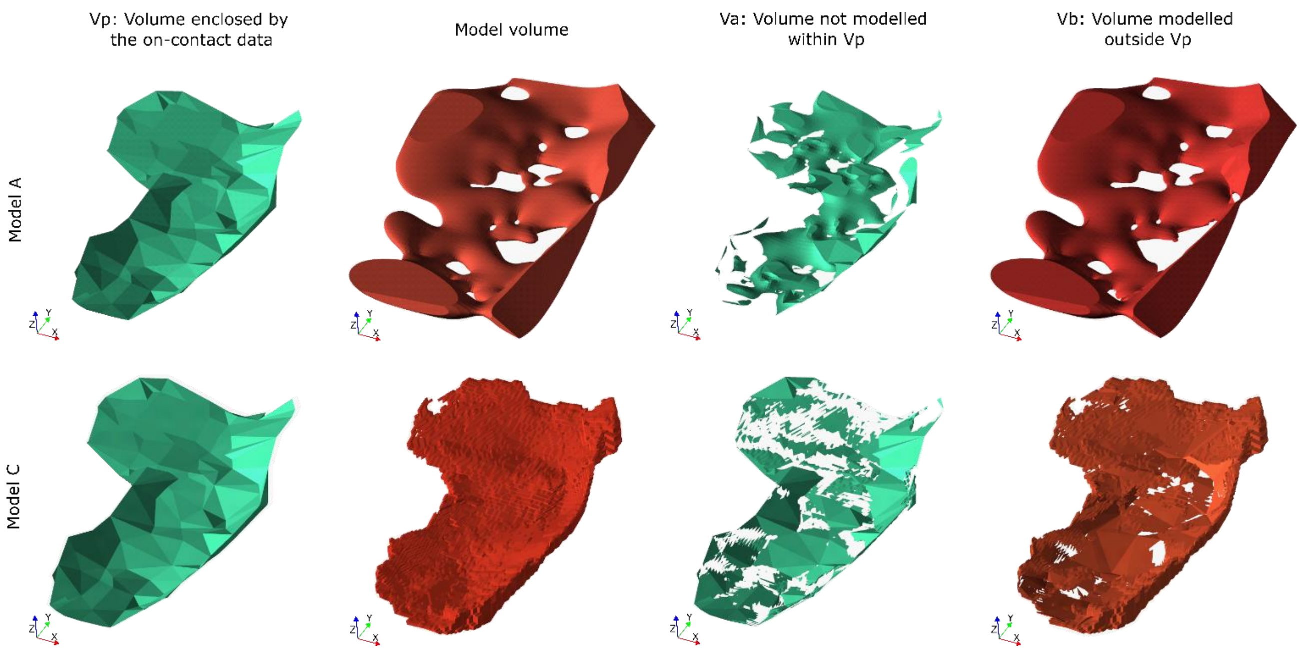

Figure 11. Volumes of Models A and C used to compute a normalized error between the geometry given by the data and the geometry given by each model.

To assess how realistic are the resulting 3D models, we compare the intrusion dimension and geometry given by the data and given by each of the models. To compare the intrusion dimension, we estimate the volume enclosed by the input contact data V_p and the volume enclosed by each model V_i, where $i=\{A, B, C, D\}$. We compute the symmetric difference between each V_i and V_p, and we estimated a normalized error as:

$$Normalized\ error = \frac{V_i^a + V_i^b}{V_p} \tag{8}$$

Where V_i^a is the volume not modelled within V_p, and V_i^b is the volume modelled outside V_p (Figure 11, Table 1). A small normalized error indicates the volumes V_i^a and V_i^b are relatively small compared to the volume enclosed by the input data V_p. The 3D models built with RBF interpolation exhibit a greater volume modelled outside V_p, resulting in a more significant normalized error. Models C and D present similar volume errors, with model C showing a slightly better figure due to the smaller volume V_C^a.

To assess the geometry of the intrusion, we visually inspect 12 cross-sections, and we measure the thickness of each model. Figure 12 shows the sections along the Y-axis. Model A shows substantial differences compared to the other models, and it does not reproduce the expected sheet-like shape of a sill, nor a clear transition from the inner to the outer sill. Models B, C and D capture the inclined geometry of the outer sills; however, model C seems to flatten the eastern inclined sheet. This is because model C's intrusion network is interpolated using the base contact points, and this interpolation does not necessarily honour the geometry of the stratigraphy and structures. As the intrusion network controls the geometry of coordinate g of the structural frame, the parameterized conceptual model and the residual values will be affected by its geometry. Models C and D are slightly better at recovering the straight top and base contacts, while model B exhibits wavy contacts in some parts of the model.

The thickness of the models is measured in pre-defined locations, and it is compared with the thickness given by the data (Figure 13). As Köpping *et al*. (2021) describe, the data shows that the intrusion thickness decreases from E to W within the inner sill and towards the tips and inclined outer sills. Model A does not show any evident trend, and the thickness is generally larger than the thickness given by the data. Model B thins down towards the western lobate termination but it does not capture the decreased thickness observed in the outer sills and the southern tip. Models C and D show a decreasing trend towards the western and southern tips but tend to amplify the difference with the data closer to the outer sills.

https://doi.org/10.5194/gmd-2022-88
Preprint. Discussion started: 22 April 2022

Geoscientific Model Development Discussions

Table 1. Input data and results of the dimension and geometric comparison between the models.

	Input data			Volume Comparison					Thickness difference	
	N° of on-contact constraints	N° of plannar or inflation constraints	Other	Model Volume [km³]	Vp [km³]	Va [km³]	Vb [km³]	Normalized error	Average	Standard Deviation
Model A	184 points	88 points	-	52.14	8.81	3.26	46.58	5.66	459.4	409.9
Model B	755 points	570 points	-	18.49	8.65	1.48	11.32	1.48	108.2	167.0
Model C	184 points	88 points	7 propagation/long axis points	13.84	8.81	2.17	7.19	1.06	50.2	109.8
Model D	184 points	88 points	14 propagation/long axis points	12.43	8.81	3.46	7.08	1.20	43.4	75.3

520

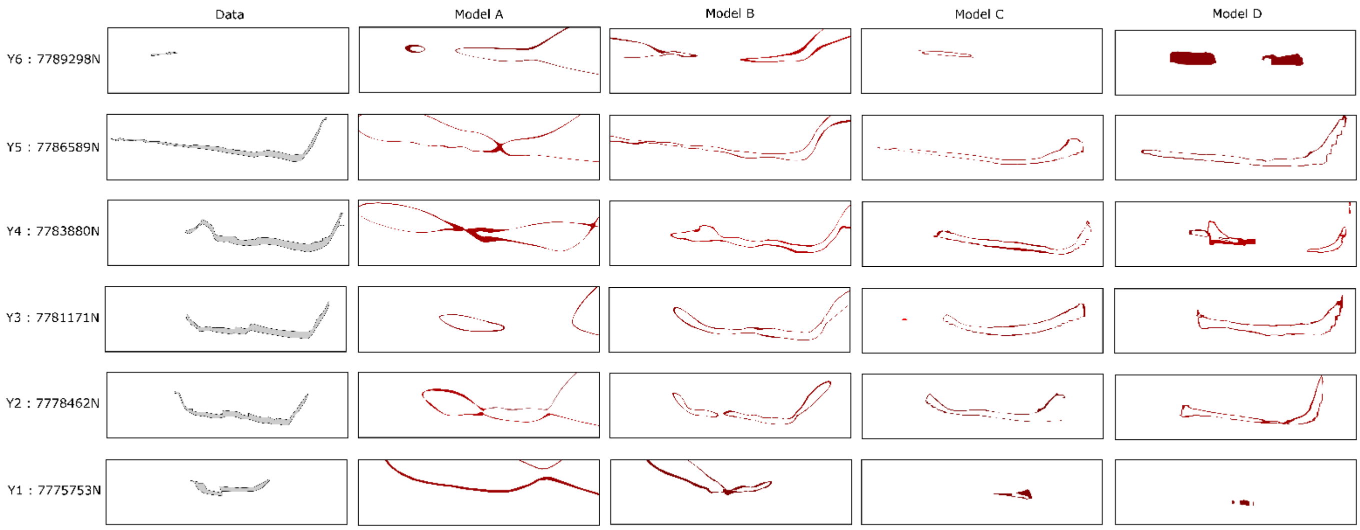

Figure 12. Comparison of the intrusion geometry between models, EW sections. The grey polygons show the geometry given by the dataset presented by Köpping et al. (2021)

https://doi.org/10.5194/gmd-2022-88
Preprint. Discussion started: 22 April 2022

Geoscientific Model Development Discussions Open Access EGU

We compute the difference between the thicknesses measured on each model and the thickness given by the data (Figure 13b, Table 1). This difference's mean and standard deviation are significantly lower in model B with respect to model A, showing the effect of adding more constraints. Model C and D have a similar mean and standard deviation, and these figures are slightly lower in model C.

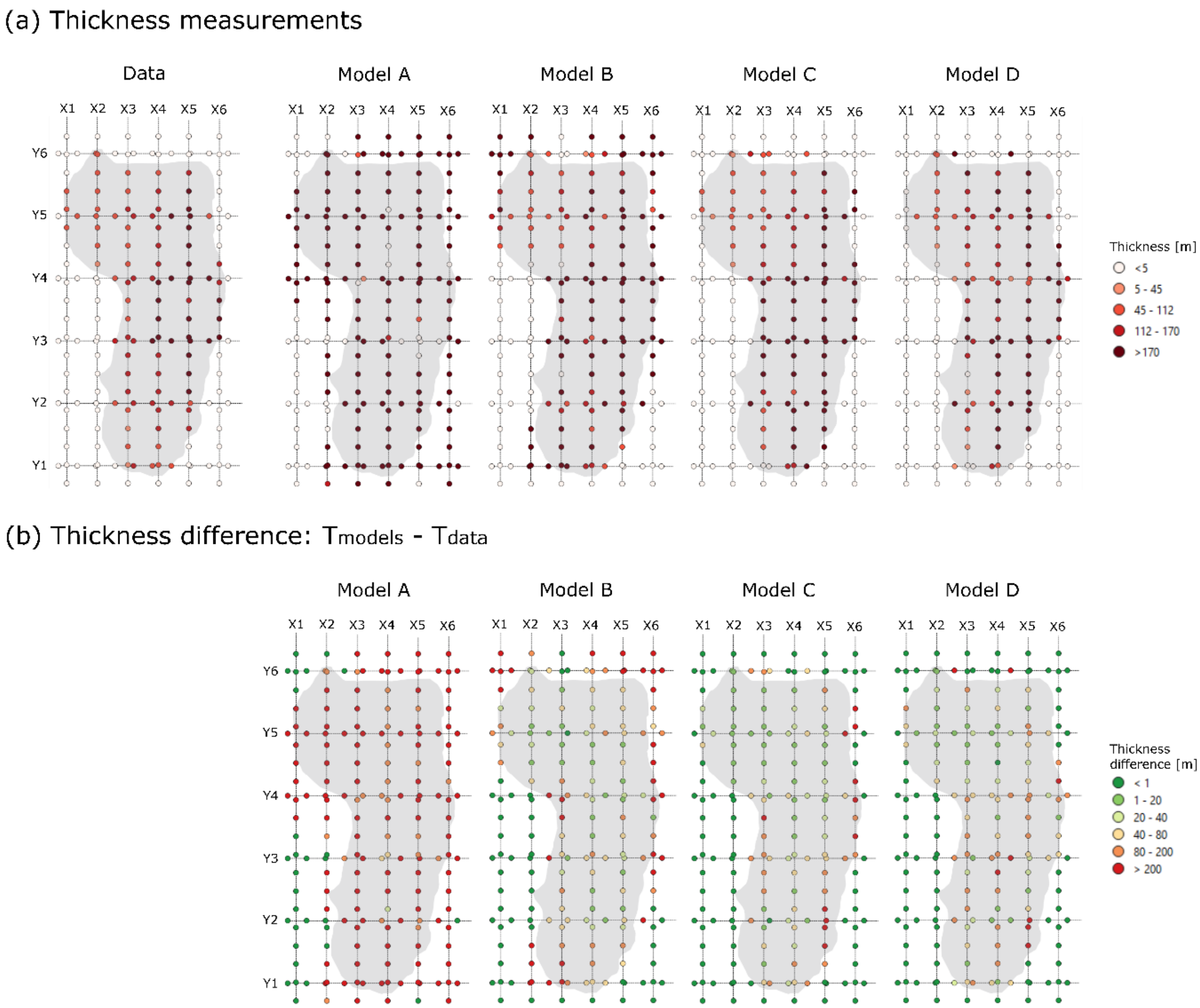

530 **Figure 13. Thickness comparison. (a) Thickness measurements along 6 NS sections and 6 EW sections. (b) Difference between thickness measurements on each model and thickness given by the data.**

6 Discussion

To date, 3D models of intrusions are built with classical interpolation workflows, where on-contact data is used to estimate boundaries. Post-processing is usually required to generate realistic shapes, making the model dependent on the modeller's expertise and challenging to reproduce. Even though such an approach is capable of honouring hard data, it cannot reproduce spatial variability. In this contribution, we have proposed a method to address these limitations by implementing the Object-Distance Simulation Method (Henrion *et al*., 2008, 2010) and a structural frame for intrusions (Laurent *et al*., 2013, 2016; Godefroy *et al*., 2017, Grose *et al*., 2021a,b). The structural frame incorporates conceptual knowledge of intrusion emplacement mechanisms into the modelling framework and uses different field measurements. It also enables the assessment of simplified intrusion morphology by providing a curvilinear coordinate system. This coordinate system allows the intrusion geometry to be visualised along its long axis. This is particularly useful for complex systems of intrusions, such as sills that step up and down within the stratigraphy, with variable propagation direction. Figure 14 shows a comparison of the thickness and width variation between the magma lobes of the CS1. This case study illustrates a synthetic sill complex comprised of three magma lobes propagating in slightly different directions. The middle sill steps up, exploiting a pre-existing structure. The P-G and P-S coordinate plots in Figure 14 show how the thickness and width of each sill vary while they propagate away from the feeder.

The Object-Distance Simulation Method allows the generated models to honour spatial variability between data points. In our method, spatial variability of the intrusion contact between the data is modelled by simulating four spatially correlated random fields that control the intrusion extent, and it is restrained using conceptual models of the expected intrusions geometries. The modeller must choose a conceptual model, which is then parameterized using the input data and the structural frame coordinates. The parameters that control the simulations are a probability of occurrence (density) and a variogram. Since the conceptual model is constrained using the input data, it is expected that the probability distribution is restricted to small values, and the variability should be low at any lag distance of the variogram. The range of probable values must be relatively small, avoiding the generation of unrealistic shapes, such as sharp changes in intrusion thickness or width. One limitation of our method is that the modeller has to determine which conceptual model to use. However, the conceptual model can be selected after assessing the data and the regional context. Also, the definition of the conceptual model would be comparable to defining a conceptual model while drawing shapes or adding arbitrary (non-quantified through proper geostatistical analysis) structural trends to the model. Having a set of possible conceptual models is objective, unbiased and enables the modeller to test different geometries. A workflow to automatically find the best fitting conceptual model can be implemented in the future. Following the approach of Grose *et al*. (2018; 2019), fitting the conceptual model to the observations can be considered as an inverse problem.

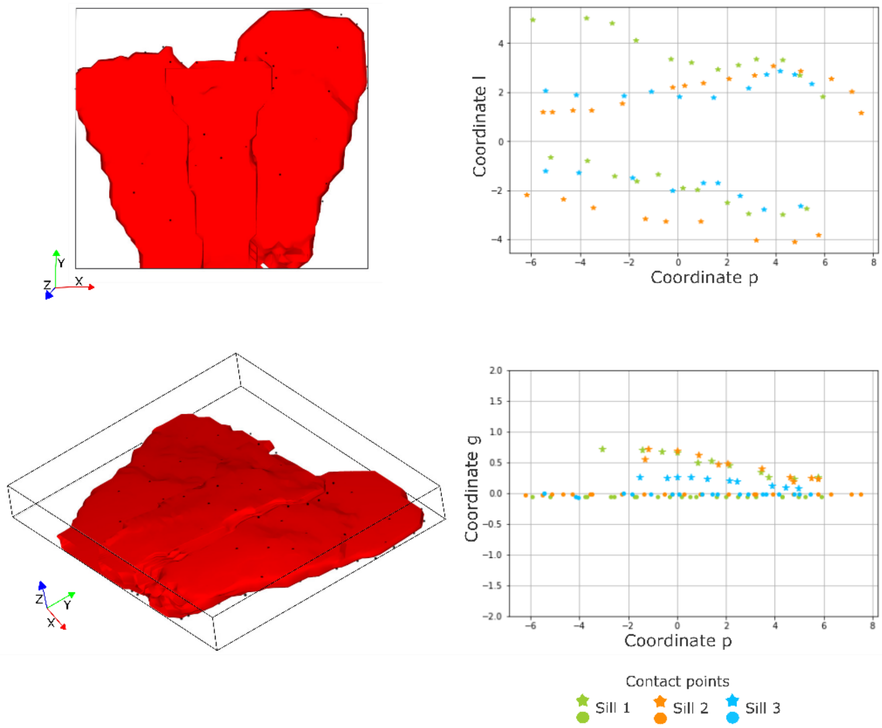

Figure 14. Synthetic sill complex model. The magma segments propagate in slightly different directions. The middle sill exploits a pre-existing structure and propagates thought a higher stratigraphic level. The segments are thicker closer to the source, and coalesce between them developing step geometries. The plots show a comparison of the thickness and width variation between the three sills.

Stochastic simulation enables the generation of several realizations that honours the same model parameters. The models after all realization can be compared and used to determine the global and local uncertainty of the model given the input data. Zones of the intrusion with higher uncertainty can be determined and prioritize for further data collection and model refinement.

In general, the 3D models of CS1 and CS2 (Figure 7 and 8) are in good agreement with natural intrusions geometries (*e.g.*,Cruden *et al*., 2017, 1999; Galland *et al*., 2018; Jackson *et al*., 2013; Kavanagh 2018; McCaffrey and Petford 1997; Vigneresse 1995; Vigneresse *et al*., 1999). The method can reproduce realistic morphologies of different types of intrusion, even with sparse datasets. Considering CS3 (Figure 10), our method reproduces more realistic sill geometries compared to RBF interpolation, especially when considering a restricted dataset, such as in models A, C and D. In particular, our method can replicate the tabular geometry of this sill intrusion, constrain its terminations and thickness variations, as well as generating a model of similar dimension, including thickness variation trends, to what is observed in contact data. Parameterization of the intrusion using the structural frame is crucial and enables a rigorous simulation of the intrusion extent in the direction in which the intrusion grew. Models C and D used a handful amount of propagation and growth direction data (see Table 1), and the

https://doi.org/10.5194/gmd-2022-88
Preprint. Discussion started: 22 April 2022

models do not need a dense dataset to produce realistic intrusion shapes. It is also possible for the modeller to add geometrical constraints knowing the emplacement history of the intrusion. For CS3 (sill intrusion in NW Australia) we were able to model the steep inclined sheets by adding marginal faults to the intrusion network workflow of model D. This type of geometry would be difficult to reproduce using a classic interpolation approach unless a large dataset were provided as in model B. However, having a dense dataset is rarely the case, and models of intrusions are usually built using sparse and unevenly distributed datasets.

The main limitation of the proposed method is that the surface representing the intrusion contact (*i.e.*, scalar field $B=0$) depends on the size of the model grid elements. Consider a part of the intrusion that is narrower or thinner than the size of a grid element, in this case, the nodes around the intrusion will indicate threshold values l^t and g^t smaller than their respective ℓ and g coordinates, and they will not be indicated as being inside the intrusion. The scalar field value on these nodes will be B>0, and therefore no isosurface B=0 will be found between them. This scenario is observed in the narrower zone of Voisey's Bay intrusion model (CS2, Figure 8). According to the data, the intrusion transitions to a narrow and thin sill-like intrusion, which the model does not capture. This is also observed in the thinnest parts of the sill intrusion in NW Australia presented in section 5 (CS3, models C and D in Figure 10). This limitation can be addressed using a higher resolution mesh, however this introduces computing limitations (time and memory usage). Adaptative meshing algorithms should also be considered in the next iteration of the implementation.

7 Conclusions

Current methods to build 3D models of igneous intrusions are strongly dependent on data availability and manual processing. They do not consider geological knowledge of intrusion emplacement mechanisms objectively and do not use all types of measurements collected in the field. In this context, the generation of realistic intrusion shapes is challenging to reproduce from one model realization to another. To address these problems, we developed a method to build 3D models of intrusions that accounts for geological knowledge, models of the host rocks and typical datasets. The method is a modified version of the Object-Distance Simulation Method (ODSIM), specifically adapted to intrusions. We incorporate an intrusion structural frame into the ODSIM framework that accounts for intrusion growth and propagation. This structural frame provides a curvilinear coordinate system for each intrusion sheet or pluton within the model. A conceptual model of the intrusion shape is parameterized using the structural frame coordinates and then stochastically perturbed using spatially correlated random fields. The conceptual models include a conceptual idea of the intrusion shape objectively, and the random fields add the expected spatial variability between the data points. The test of different scenarios using different conceptual models can be performed without the modeller's bias, and models can be reproduced for further assessments. Fitting of all the data is not always feasible and may be dependent on the grid size. Further work on the method will include automatically fitting the conceptual models to the data and adaptative meshes to improve the intrusion resolution.

Code and data availability

The examples presented in this contribution were generated using the open source 3D modelling package LoopStructural. LoopStructural v.1.4.4 can be downloaded from https://doi.org/10.5281/zenodo.6381007 or installed using pip install LoopStructural. The input data and Jupyter notebooks of all the examples presented in this work can be downloaded from https://doi.org/10.5281/zenodo.6381034

Author contributions

All authors contributed to the conceptual design of the method and comparative analyses presented in this work. FAN developed the model code with editing and improvements contributions from LG. FAN prepared the manuscript with editing and reviewing contributions from all co-authors.

Acknowledgements

Funding was provided by ARC Linkage grant LP17010985 – Enabling 3D Stochastic Geological Modelling; supporting the development of the Loop platform. Ms Alvarado is funded by Monash International Tuition Scholarship. The authors would like to thank Jonas Köpping for providing the data of case study 3.

References

Barnett, Z. A. and Gudmundsson, A.: Numerical modelling of dykes deflected into sills to form a magma chamber, J. Volcanol. Geotherm. Res., 281, 1–11, https://doi.org/10.1016/j.jvolgeores.2014.05.018, 2014.

Borghi, A., Renard, P., and Jenni, S.: A pseudo-genetic stochastic model to generate karstic networks, J. Hydrol., 414–415, 516–529, https://doi.org/10.1016/j.jhydrol.2011.11.032, 2012.

Braga, F. C. S., Rosiere, C. A., Santos, J. O. S., Hagemann, S. G., and Salles, P. V.: Depicting the 3D geometry of ore bodies using implicit lithological modeling: An example from the Horto-Baratinha iron deposit, Guanhães block, MG, REM - Int. Eng. J., 72, 435–443, https://doi.org/10.1590/0370-44672018720167, 2019.

Brown, M.: Crustal melting and melt extraction, ascent and emplacement in orogens: mechanisms and consequences, J. Geol. Soc. London., 164, 709–730, https://doi.org/10.1144/0016-76492006-171, 2007a.

Brown, M.: Crustal melting and melt extraction, ascent and emplacement in orogens: Mechanisms and consequences, J. Geol. Soc. London., 164, 709–730, https://doi.org/10.1144/0016-76492006-171, 2007b.

Brun, J. P. and Pons, J.: Strain patterns of pluton emplacement in a crust undergoing non-coaxial deformation, Sierra Morena, Southern Spain, J. Struct. Geol., 3, 219–229, https://doi.org/10.1016/0191-8141(81)90018-3, 1981.

Burchardt, S.: Introduction to volcanic and igneous plumbing systems-developing a discipline and common concepts, Elsevier

https://doi.org/10.5194/gmd-2022-88
Preprint. Discussion started: 22 April 2022

Inc., 1–12 pp., https://doi.org/10.1016/B978-0-12-809749-6.00001-7, 2018.

Caumon, G., Gray, G., Antoine, C., and Titeux, M.-O.: Three-Dimensional Implicit Stratigraphic Model Building From Remote Sensing Data on Tetrahedral Meshes: Theory and Application to a Regional Model of La Popa Basin, NE Mexico, IEEE Trans. Geosci. Remote Sens., 51, 1613–1621, https://doi.org/10.1109/TGRS.2012.2207727, 2013.

Cervantes, C. A.: 3D Modelling of Faulting and Intrusion of the Nevado del Ruiz Volcano , Colombia, Reykjavík University, 2019.

Clausolles, N., Collon, P., and Caumon, G.: Generating variable shapes of salt geobodies from seismic images and prior geological knowledge, 7, T829–T841, https://doi.org/10.1190/int-2019-0032.1, 2019.

Clemens, J. D. and Mawer, C. K.: Granitic magma transport by fracture propagation, 204, 339–360, https://doi.org/10.1016/0040-1951(92)90316-X, 1992.

Cruden, A.: On the emplacement of tabular granites, J. Geol. Soc. London., 155, 853–862, https://doi.org/10.1144/gsjgs.155.5.0853, 1998.

Cruden, A. R.: Emplacement and growth of plutons: implications for rates of melting and mass transfer in continental crust, in: Evolution and Differentiation of the Continental Crust, edited by: Michael Brown, T. R., Cambridge University Press, Cambridge UK, 455–519, 2006.

Cruden, A. R. and McCaffrey, K. J. W.: Growth of plutons by floor subsidence: implications for rates of emplacement, intrusion spacing and melt-extraction mechanisms, Phys. Chem. Earth, Part A Solid Earth Geod., 26, 303–315, https://doi.org/10.1016/S1464-1895(01)00060-6, 2001.

Cruden, A. R. and Weinberg, R. F.: Mechanisms of Magma Transport and Storage in the Lower and Middle Crust—Magma Segregation, Ascent and Emplacement, in: Volcanic and Igneous Plumbing Systems, Elsevier, 13–53, https://doi.org/10.1016/B978-0-12-809749-6.00002-9, 2018.

Cruden, A. R., Sjöström, H., and Aaro, S.: Structure and geophysics of the Gåsborn granite, central Sweden: an example of fracture-fed asymmetric pluton emplacement, Geol. Soc. London, Spec. Publ., 168, 141–160, https://doi.org/10.1144/GSL.SP.1999.168.01.10, 1999.

Cruden, A. R., McCaffrey, K. J. W., and Bunger, A. P.: Geometric Scaling of Tabular Igneous Intrusions: Implications for and, in: Physical Geology of Shallow Magmatic Systems, vol. 104, edited by: Breitkreuz, C. and Rocci, S., Springer, Switzerland, 11–38, https://doi.org/10.1007/11157_2017_1000, 2017.

Deutsch, C. V. and Journel, A. G.: GSLIB: geostatistical software library and user's guide. Second edition, 1998.

Eshaghi, E., Reading, A. M., Roach, M., Cracknell, M. J., Duffett, M., Bombardieri, D., and Tasmania, M. R.: 3D modelling of granite intrusions in northwest tasmania using petrophysical and residual gravity data, SEG Tech. Progr. Expand. Abstr., 35, 1637–1642, https://doi.org/10.1190/segam2016-13780273.1, 2016.

Frank, T., Tertois, A., and Mallet, J.: Implicit reconstruction of complex geological surfaces, 1–20, 2005.

Frank, T., Tertois, A. L., and Mallet, J. L.: 3D-reconstruction of complex geological interfaces from irregularly distributed and noisy point data, Comput. Geosci., 33, 932–943, https://doi.org/10.1016/j.cageo.2006.11.014, 2007a.

https://doi.org/10.5194/gmd-2022-88
Preprint. Discussion started: 22 April 2022

Frank, T., Tertois, A.-L., and Mallet, J.-L.: 3D-reconstruction of complex geological interfaces from irregularly distributed and noisy point data, Comput. Geosci., 33, 932–943, https://doi.org/10.1016/j.cageo.2006.11.014, 2007b.

Galland, O., Bertelsen, H. S., Eide, C. H., Guldstrand, F., Haug, T., Leanza, H. A., Mair, K., Palma, O., Planke, S., Rabbel, O., Rogers, B., Schmiedel, T., Souche, A., and Spacapan, J. B.: Storage and transport of magma in the layered crust-formation of sills and related flat-lying intrusions, Elsevier Inc., 113–138 pp., https://doi.org/10.1016/B978-0-12-809749-6.00005-4, 2018.

Godefroy, G., Laurent, G., Caumon, G., and Walter, B.: A Parametric Unfault-and-refault Method for Chronological Structural Modeling, https://doi.org/10.3997/2214-4609.201701146, 2017.

Godefroy, G., Caumon, G., Ford, M., Laurent, G., and Jackson, C. A. L.: A parametric fault displacement model to introduce kinematic control into modeling faults from sparse data, 6, B1–B13, https://doi.org/10.1190/INT-2017-0059.1, 2018.

Grocott, J., Garde, A. A., Chadwick, B., Cruden, A. R., and Swager, C.: Emplacement of rapakivi granite and syenite by floor depression and roof uplift in the Palaeoproterozoic Ketilidian orogen, South Greenland, J. Geol. Soc. London., 156, 15–24, https://doi.org/10.1144/gsjgs.156.1.0015, 1999.

Grose, L., Laurent, G., Aillères, L., Armit, R., Jessell, M., and Caumon, G.: Structural data constraints for implicit modeling of folds, J. Struct. Geol., 104, 80–92, https://doi.org/10.1016/j.jsg.2017.09.013, 2017a.

Grose, L., Laurent, G., Aillères, L., Armit, R., Jessell, M., and Caumon, G.: Structural data constraints for implicit modeling of folds, J. Struct. Geol., 104, 80–92, https://doi.org/10.1016/j.jsg.2017.09.013, 2017b.

Grose, L., Laurent, G., Aillères, L., Armit, R., Jessell, M., and Cousin-Dechenaud, T.: Inversion of Structural Geology Data for Fold Geometry, J. Geophys. Res. Solid Earth, 123, 6318–6333, https://doi.org/10.1029/2017JB015177, 2018.

Grose, L., Ailleres, L., Laurent, G., Armit, R., and Jessell, M.: Inversion of geological knowledge for fold geometry, J. Struct. Geol., 119, 1–14, https://doi.org/10.1016/j.jsg.2018.11.010, 2019.

Grose, L., Aillères, L., Laurent, G., and Jessell, M.: Loop3D/LoopStructural-v1.3.10.zip, https://doi.org/10.5281/zenodo.5664333, 2020.

Grose, L., Ailleres, L., Laurent, G., and Jessell, M.: LoopStructural 1.0: time-aware geological modelling, Geosci. Model Dev., 14, 3915–3937, https://doi.org/10.5194/gmd-14-3915-2021, 2021a.

Grose, L., Ailleres, L., Laurent, G., Caumon, G., Jessell, M., and Armit, R.: Realistic modelling of faults in LoopStructural 1.0, Geosci. Model Dev. Discuss., 2021, 1–26, https://doi.org/10.5194/gmd-2021-112, 2021b.

Grose, L., Ailleres, L., Laurent, G., Caumon, G., Jessell, M., and Armit, R.: Realistic modelling of faults in LoopStructural 1 . 0, 1–26, https://doi.org/https://doi.org/10.5194/gmd-2021-112, 2021c.

Gudmundsson, A.: Deflection of dykes into sills at discontinuities and magma-chamber formation, 500, 50–64, https://doi.org/10.1016/j.tecto.2009.10.015, 2011.

Guineberteau, B., Bouchez, J. L., and Vigneresse, J. L.: The Mortagne granite pluton (France) emplaced by pull-apart along a shear zone: Structural and gravimetric arguments and regional implication, Geol. Soc. Am. Bull., 99, 763, https://doi.org/10.1130/0016-7606(1987)99<763:TMGPFE>2.0.CO;2, 1987.

https://doi.org/10.5194/gmd-2022-88
Preprint. Discussion started: 22 April 2022

Haldorsen, H. H. and Damsieth, E.: Stochastic modeling, SPE Repr. Ser., 65–73, https://doi.org/10.1201/9781315370309-12, 1990.

Henrion, V., Pellerin, J., Caumon, G., Henrion, V., Pellerin, J., Caumon, G., and Methodology, A. S.: A Stochastic Methodology for 3D Cave Systems Modeling To cite this version : HAL Id : hal-01844418, 2008.

Henrion, V., Caumon, G., and Cherpeau, N.: ODSIM: An Object-Distance Simulation Method for Conditioning Complex Natural Structures, Math. Geosci., 42, 911–924, https://doi.org/10.1007/s11004-010-9299-0, 2010.

Hillier, M. J., Schetselaar, E. M., de Kemp, E. A., and Perron, G.: Three-Dimensional Modelling of Geological Surfaces Using Generalized Interpolation with Radial Basis Functions, Math. Geosci., 46, 931–953, https://doi.org/10.1007/s11004-014-9540-3, 2014.

Hogan, J. P. and Gilbert, M. C.: The A-type Mount Scott Granite sheet: Importance of crystal magma traps, J. Geophys. Res. Solid Earth, 100, 15779–15792, https://doi.org/10.1029/94JB03258, 1995.

Hutton, D. H. W.: Granite emplacement mechanisms and tectonic controls: inferences from deformation studies, Earth Environ. Sci. Trans. R. Soc. Edinburgh, 79, 245–255, https://doi.org/10.1017/S0263593300014255, 1988a.

Hutton, D. H. W.: Igneous emplacement in a shear-zone termination: The biotite granite at Strontian, Scotland, Geol. Soc. Am. Bull., 100, 1392–1399, https://doi.org/10.1130/0016-7606(1988)100<1392:IEIASZ>2.3.CO;2, 1988b.

Hutton, D. H. W.: Insights into magmatism in volcanic margins: Bridge structures and a new mechanism of basic sill emplacement - Theron Mountains, Antarctica, Pet. Geosci., 15, 269–278, https://doi.org/10.1144/1354-079309-841, 2009.

Irakarama, M., Laurent, G., Renaudeau, J., and Caumon, G.: Finite Difference Implicit Structural Modeling of Geological Structures, Math. Geosci., https://doi.org/10.1007/s11004-020-09887-w, 2020.

Jackson, C. A. L., Schofield, N., and Golenkov, B.: Geometry and controls on the development of igneous sill-related forced folds: A 2-D seismic reflection case study from offshore southern Australia, Geol. Soc. Am. Bull., 125, 1874–1890, https://doi.org/10.1130/B30833.1, 2013.

Jessell, M. W., Ailleres, L., and de Kemp, E. A.: Towards an integrated inversion of geoscientific data: What price of geology?, 490, 294–306, https://doi.org/10.1016/j.tecto.2010.05.020, 2010.

Jones, M. W., Bærentzen, J. A., and Sramek, M.: 3D distance fields: A survey of techniques and applications, IEEE Trans. Vis. Comput. Graph., 12, 581–599, https://doi.org/10.1109/TVCG.2006.56, 2006.

Kavanagh, J. L.: Mechanisms of magma transport in the upper crust-dyking, Elsevier Inc., 55–88 pp., https://doi.org/10.1016/B978-0-12-809749-6.00003-0, 2018a.

Kavanagh, J. L.: Mechanisms of Magma Transport in the Upper Crust—Dyking, in: Volcanic and Igneous Plumbing Systems, Elsevier, 55–88, https://doi.org/10.1016/B978-0-12-809749-6.00003-0, 2018b.

Kavanagh, J. L., Menand, T., and Sparks, R. S. J.: An experimental investigation of sill formation and propagation in layered elastic media, Earth Planet. Sci. Lett., 245, 799–813, https://doi.org/10.1016/j.epsl.2006.03.025, 2006.

Köpping, J., Magee, C., Cruden, A. R., Jackson, C. A.-L., and Norcliffe, J.: The building blocks of igneous sheet intrusions: insights from 3D seismic reflection data, https://doi.org/https://doi.org/10.31223/X5659D, 2021.

Laurent, G., Caumon, G., Bouziat, A., and Jessell, M.: A parametric method to model 3D displacements around faults with volumetric vector fields, 590, 83–93, https://doi.org/10.1016/j.tecto.2013.01.015, 2013.

Laurent, G., Ailleres, L., Grose, L., Caumon, G., Jessell, M., and Armit, R.: Implicit modeling of folds and overprinting deformation, Earth Planet. Sci. Lett., 456, 26–38, https://doi.org/10.1016/j.epsl.2016.09.040, 2016.

Magee, C., Muirhead, J. D., Karvelas, A., Holford, S. P., Jackson, C. A. L., Bastow, I. D., Schofield, N., Stevenson, C. T. E., McLean, C., McCarthy, W., and Shtukert, O.: Lateral magma flow in mafic sill complexes, 12, 809–841, https://doi.org/10.1130/GES01256.1, 2016.

Magee, C., Muirhead, J., Schofield, N., Walker, R. J., Galland, O., Holford, S., Spacapan, J., Jackson, C. A.-L., and McCarthy, W.: Structural signatures of igneous sheet intrusion propagation, J. Struct. Geol., 125, 148–154, https://doi.org/10.1016/j.jsg.2018.07.010, 2019.

McCaffrey, K. J. W. and Petford, N.: Are granitic intrusions scale invariant?, J. Geol. Soc. London., 154, 1–4, https://doi.org/10.1144/gsjgs.154.1.0001, 1997.

Morgan, S.: Pascal's Principle, a Simple Model to Explain the Emplacement of Laccoliths and Some Mid-crustal Plutons, Elsevier Inc., 139–165 pp., https://doi.org/10.1016/B978-0-12-809749-6.00006-6, 2018.

Petford, N., Cruden, A. R., McCaffrey, K. J. W., and Vigneresse, J. L.: Granite magma formation, transport and emplacement in the Earth's crust, Nature, 408, 669–673, https://doi.org/10.1038/35047000, 2000.

Rawling, T. J., Osborne, C. R., McLean, M. A., Skladzien, P. B., Cayley, R. A., and Williams, B.: 3D Victoria Final Report, Geosci. Victoria 3D Victoria Rep., 1–98, 2011.

Rongier, G., Collon-Drouaillet, P., and Filipponi, M.: Simulation of 3D karst conduits with an object-distance based method integrating geological knowledge, 217, 152–164, https://doi.org/10.1016/j.geomorph.2014.04.024, 2014.

Saumur, B. M. and Cruden, A. R.: On the emplacement of the Voisey's Bay intrusion (Labrador, Canada), Geol. Soc. Am. Bull., 128, B31240.1, https://doi.org/10.1130/B31240.1, 2015.

Schofield, N. J., Brown, D. J., Magee, C., and Stevenson, C. T.: Sill morphology and comparison of brittle and non-brittle emplacement mechanisms, J. Geol. Soc. London., 169, 127–141, https://doi.org/10.1144/0016-76492011-078, 2012.

Sethian, J. A.: Fast Marching Methods, SIAM Rev., 41, 199–235, https://doi.org/10.1137/S0036144598347059, 1999.

Souche, A., Galland, O., Haug, Ø. T., and Dabrowski, M.: Impact of host rock heterogeneity on failure around pressurized conduits: Implications for finger-shaped magmatic intrusions, 765, 52–63, https://doi.org/10.1016/j.tecto.2019.05.016, 2019.

Thibert, B., Gratier, J. P., and Morvan, J. M.: A direct method for modeling and unfolding developable surfaces and its application to the Ventura Basin (California), J. Struct. Geol., 27, 303–316, https://doi.org/10.1016/j.jsg.2004.08.011, 2005.

Vigneresse, J. L.: Control of granite emplacement by regional deformation, 249, 173–186, https://doi.org/10.1016/0040-1951(95)00004-7, 1995.

Vigneresse, J. L., Tikoff, B., and Améglio, L.: Modification of the regional stress field by magma intrusion and formation of tabular granitic plutons, 302, 203–224, https://doi.org/10.1016/S0040-1951(98)00285-6, 1999.

Weinberg, R. F., Sial, A. N., and Mariano, G.: Close spatial relationship between plutons and shear zones, Geology, 32, 377–

https://doi.org/10.5194/gmd-2022-88
Preprint. Discussion started: 22 April 2022

380, https://doi.org/10.1130/G20290.1, 2004a.

Weinberg, R. F., Sial, A. N., and Mariano, G.: Close spatial relationship between plutons and shear zones, Geology, 32, 377, https://doi.org/10.1130/G20290.1, 2004b.

Wellmann, F. and Caumon, G.: 3-D Structural geological models: Concepts, methods, and uncertainties, in: Advances in Geophysics, vol. 59, Elsevier Inc., 1–121, https://doi.org/10.1016/bs.agph.2018.09.001, 2018.

van Wyk de Vries, B. and van Wyk de Vries, M.: Tectonics and volcanic and igneous plumbing systems, Elsevier Inc., 167–189 pp., https://doi.org/10.1016/B978-0-12-809749-6.00007-8, 2018.